Can Traditional Chinese Medicine provide insights into controlling the COVID-19 pandemic: Serpentinization-induced lithospheric long-wavelength magnetic anomalies in Proterozoic be...

Preprint · March 2020

DOI: 10.13140/RG.2.2.30887.09128

CITATIONS
0

READS
6,518

1 author:

Moses T Bility
University of Pittsburgh
40 PUBLICATIONS **1,154** CITATIONS

SEE PROFILE

Can Traditional Chinese Medicine provide insights into controlling the COVID-19 pandemic: Serpentinization-induced lithospheric long-wavelength magnetic anomalies in Proterozoic bedrocks in a weakened geomagnetic field mediate the aberrant transformation of biogenic molecules in COVID-19 via magnetic catalysis

Author: Moses Turkle Bility[1*], Yash Agarwal[1], Sara Ho[1], Isabella Castronova[1], Cole Beatty[1], Shivkumar Biradar[1], Vanshika Narala[1], Nivitha Periyapatna[1], Yue Chen[1], and Jean Nachega[1,2]

Author Affiliation: [1]Department of Infectious Diseases and Microbiology, [2]Department of Epidemiology, Graduate School of Public Health, University of Pittsburgh, Pittsburgh, Public Health, 130 DeSoto Street, Pittsburgh, PA 15261.

***Corresponding Author:** E-mail: mtbility@pitt.edu, Primary Phone: 412-648-8058, Fax number: 412-383-8926.

Running title: Geomagnetic field dynamics modulate the COVID-19 pandemic.

Keywords: Geomagnetic field, Lithospheric magnetic field, Coronavirus virus disease, COVID-19, Emerging epidemics/pandemics.

Highlights

• Lethal COVID-19-like disease with SARS-CoV-2-like infection in a rat colony.

• Severe COVID-19 outbreaks are coupled to serpentinization-associated water dynamics.

• Severe COVID-19 outbreaks are coupled with magnetic anomalies in Proterozoic cratons.

• The COVID-19 pandemic is coupled to dynamics in the geosphere via magnetic catalysis.

• Nephrite-Jade amulets, a calcium-ferromagnesian silicate, may prevent COVID-19.

Abstract

Thoracic organs, namely, the lungs and kidneys in severe acute respiratory syndrome coronavirus 2 (SARS-CoV-2)-associated coronavirus disease 2019 (COVID-19), exhibit silicate/glass-like (hyaline) and iron oxides-like deposits, which are like serpentinization-induced minerals. The discovery of the chiral-induced spin selectivity effect suggests that a resonant external magnetic field could alter the spin state of biogenic molecules and result in the magnetic catalysis of aberrant molecules and disease. We proposed that carbon dioxide-rich water-peridotite (a ferromagnesian silicate) interactions generate abnormal lithospheric long-wavelength magnetic anomalies (LWMAs) via serpentinization, during conditions with increased terrestrial water storage and atmospheric carbon dioxide, and a weakened geomagnetic field. We provide evidence supporting a hypothesis, which posits, COVID-19 is a pathologic manifestation of resonant LWMAs-induced magnetic catalysis of iron oxides-silicate-like minerals from biogenic molecules and the coronavirus from endogenous viral elements, with the virus particles capable of replication and transmission to other hosts. We propose that those LWMAs are associated with the production of iron oxides-silicate rock minerals in tectonic plates with Proterozoic cratons. Thus, severe COVID-19 outbreaks are/will predominately occur in Eurasia and the Americas and are governed by the spatiotemporal dynamics of terrestrial water storage and the semiannual oscillation of the weakening geomagnetic magnetic field. We propose that the ferromagnetic-like iron stores in humans are the unifying determinant for COVID-19-induced morbidity and mortality. Furthermore, we propose that Nephrite-Jade amulets (a calcium-ferromagnesian silicate) developed by Neolithic Chinese Medicine to prevent thoracic organ disease, may prevent COVID-19.

Graphical Abstract

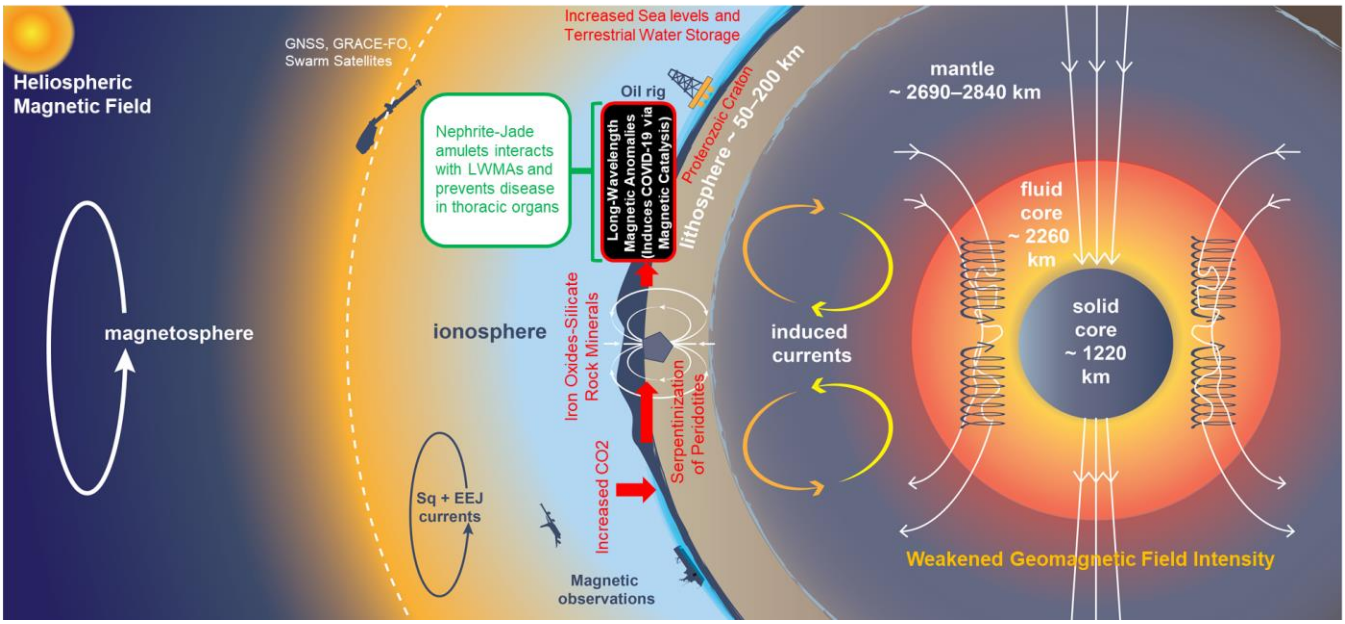

1. Introduction

Recent evidence demonstrated that megafauna (including Hominidae) die-offs in North America and Eurasia were associated with geomagnetic field intensity minima [1]. The Neolithic population collapse (~5500 before present (BP) years), which occurred over approximately 500 years in the mid-Holocene (~7000 to 5000 BP), was temporally coupled to the last geomagnetic field intensity minimum [2-7]. M.H. Walczak et al. 2017 demonstrated that the geomagnetic field secular variation in the Holocene is governed by the variable strength of the North American and Eurasian geomagnetic flux lobes at the core-mantle boundary region [8], which in turn are modulated by hydromagnetic dynamics and perturbations in the South Atlantic Anomaly [9]. Perturbations in the geodynamo are coupled to mantle dynamics, which modulates changes in lithospheric mantle rock-water interactions and atmospheric carbon dioxide levels [10-12]. The geologic and geophysical conditions of the mid-Holocene are similar to the current conditions of the Holocene, namely, increased atmospheric carbon dioxide levels [13, 14], polar ice melt-induced increased sea levels [15-17] and terrestrial water storage [18] and increased serpentinization (weathering) of peridotites in the lithospheric mantle [19, 20] in a weakened geomagnetic field [4]. This increased serpentinization of peridotites (a ferromagnesian silicate) sequesters excess atmospheric carbon dioxide into lithospheric rock minerals, generates lithospheric iron oxides-silicate rocks and associated magnetic anomalies [21, 22], and restores the carbonate-silicate geochemical cycle homeostasis [23, 24]. In a weakening geomagnetic field, the interplanetary magnetic field (heliospheric magnetic field) increasingly influences the spin state of serpentinization-derived ferromagnetic-like (ferrimagnetic) iron oxides-silicate rocks deposited in the lithosphere [25].

Many Neolithic-derived Indigenous Knowledge posits that severe geophysical-geologic perturbations and associated rock minerals play a significant role in human health [26-30]. Indeed, Neolithic-Traditional Chinese Medicine in the Hemudu and Majiabang-Neolithic Chinese cultures (~7500 to 5300 BP) [31-33] in the Yangtze River basin, on the Yangtze craton (a Proterozoic craton) in Eastern Eurasia, developed the use of the calcium-ferromagnesian silicate-Nephrite (a metasomatic derivative of serpentinization-induced rock minerals [34], commonly referred to as jade) as a disease prevention device (amulet) in the mid-Holocene during the Neolithic population collapse [7, 31, 35]. Similar Nephrite-Jade-based Neolithic cultures were developed in across Western Eurasia (Europe) during the Neolithic population collapse [36-43]. It is posited that Jade (including Nephrite) amulets protect the wearer against unseen nefarious forces that cause disease in thoracic organs [31, 32, 35]. Indeed, the romantic language word, *piedra de ijada* (from which the English word Jade is derived) translates to the stone that prevents disease in organs in the side/flank of the body (thoracic organs). Additionally, the English word Nephrite is derived from the Greek word *lapis nephriticus*, which translates to the stone that cures kidney disease.

In late 2019, a severe acute respiratory disease with multiple thoracic organ pathology and infection with the severe acute respiratory syndrome coronavirus 2 (SARS-CoV-2), termed Coronavirus disease 2019 (COVID-19), was first recorded in humans [44] in the Yangtze River basin (Wuhan, China) on the Yangtze craton [45]. The resulting SARS-CoV-2-associated COVID-19 pandemic disproportionally affects males [46-48], much like the Neolithic population collapse [49]. The lungs and kidneys in COVID-19 exhibit a silicate/glass-like (hyaline) pathology, with iron oxides-like deposits [48, 50-55], which are like serpentinization-induced

rock minerals. However, the impact of the current geological-geochemical perturbations and the weakening geomagnetic field intensity on the COVID-19 pandemic has not been explored.

The discovery of the chiral-induced spin selectivity effect in biological molecules suggests that an external magnetic field could alter the spin state of biomolecules and result in the magnetic catalysis of aberrant molecules and associated pathology in humans and other animals; however, the role of magnetic catalysis in a pandemic has not been explored [56-58]. Indeed, Naaman et al. recently demonstrated that chiral biomolecules-ferromagnetic interfaces mediate spin polarization-induced enantioselective crystallization of biological molecules [58, 59]. These developments highlight the need for an interdisciplinary analysis of the “unseen nefarious force-induced disease” hypothesis, posited by Neolithic-Traditional Chinese Medicine [26, 31, 32] and other Indigenous Knowledge [27], which takes into consideration the chiral-induced spin selectivity effect and magnetic catalysis [60-70].

The dominant paradigm for describing virus-associated pandemics, including the SARS-CoV-2-associated COVID-19 pandemic, is the germ theory [71]. The germ theory and its derivatives posit that transmissible, replication-competent, exogenous viruses (i.e., SARS-CoV-2) either directly or indirectly (via inflammation) mediate disease in virus-associated epidemics and pandemics [71]. The germ theory is based on classical electrostatics; therefore, purtubations in the spin state of biogenic molecules are assumed to be unimportant, and relevant concepts (i.e., chiral-induced spin selectivity) in condensed matter physics are ignored. The germ theory was introduced in the late 19th century and subsequently displaced most Indigenous knowledge systems [28-30]. Although the germ theory is the current dominant paradigm and

exhibits an explanatory and predictive capacity for many features of the phenomenology of virus-associated epidemics and pandemics, many significant features are unaccounted for in this theory. Many respiratory virus-associated outbreaks (i.e., influenza outbreaks) exhibit a spatiotemporal dynamic that is couple to calendar dynamics and associated geographic restrictions, despite increased intra-regional and global travel in the 21st century [72-76]. Additionally, the COVID-19 pandemic mimics a vibrating drumhead-like oscillation across the globe, in contrast to the predicted near-simultaneous severe global outbreaks posited by the germ theory [77, 78]. Importantly, the phenomenology of the SARS-CoV-2-associated COVID-19 pandemic has contradicted the germ theory-derived prediction that the severity of the outbreaks (based on deaths per million people) would be relatively higher in regions with relatively weak public health systems (i.e., Africa), as compared to regions with relatively strong health systems (i.e., North America and Western Eurasia) [78]. This discordancy cannot be reconciled globally by risk factors (i.e., elderly population) associated with COVID-19-induced mortality, ancestral differences (or the so-called genetic differences), molecular diagnostics capacity, or climate differences [79]. Indeed, Mbow M et al., 2020 showed analysis that incorporates age demographics, surveillance of acute health emergencies, and the number of tests per confirm COVID-19 cases do not account for the discordance between the germ theory-derived prediction and the actual outcome in regions with relatively strong health systems and those with weak health systems [79]. Furthermore, Japan, which lies outside Western Eurasia, has the highest percentage of the elderly population; however, Japan has not experienced a severe COVID-19 outbreak [80]. Indeed, this anomaly within the germ theory occurred in Japan despite receiving a large percentage of the travelers from the Yangtze River basin (including Wuhan) at the onset of the pandemic and implementing limited

social distancing interventions [77, 80]. This anomaly within the germ theory paradigm for the COVID-19 outbreaks in Japan is currently ascribed to the so-called “unknown Japanese X factor” [81]. Additionally, countries on the South American plate with relatively young populations (i.e., Peru, Ecuador) have experienced severe COVID-19 outbreaks [82-84]. Although regions with weak health systems have a relatively lower molecular diagnostic capacity, syndromic surveillance is employed globally [85-89]; thus, deaths due to an emerging, severe acute respiratory disease is captured uniformly across time and different countries, irrespective of national wealth [79]. Tropical (warmer) climate per se does not affect the severity of the COVID-19 pandemic [90, 91]. Although tropical countries on the African, Indian, and Eurasian plates have experienced relatively less severe COVID-19 outbreaks, tropical countries on the South American plate have experienced severe COVID-19 outbreaks [91]. Populations with African ancestry have the highest COVID-19-mortality burden in North America [92, 93] and parts of Western Eurasia [94], albeit, Africans have the lowest COVID-19-mortality burden [79]; thus creating the African ancestry-COVID-19 paradox.

A major unanswered question in the germ theory of virus-associated pandemics, including the SARS-CoV-2-associated COVID-19 pandemic, is the origin of the so-called emerging viruses. The germ theory-derived hypothesis posits that emerging virus-associated pandemics result from a spill-over of viruses from wildlife into humans (the zoonosis hypothesis), with the calender-associated dynamics of the so-called spill-over events due to the seasonality of human activities in wildlife habitat. However, the recent discovery of the genetic fragments of many non-retroviruses, including the so-called emerging viruses, in the genomes of humans and many terrestrial animals raises concerns about the validity of that hypothesis [95-97].

Calendar dynamics are a manifestation of geophysical dynamics, and those geophysical forces are manifested differently at various locations; thus, suggesting that geophysical forces could mediate the virus-associated pandemics.

Here, using insights from Traditional Chinese Medicine and other Indigenous Knowledge, we evaluate the hypothesis, which posits, SARS-CoV-2-associated COVID-19 outbreaks are mediated by serpentinization-induced resonant long-wavelength magnetic anomalies (LWMAs) in tectonic plates with Proterozoic cratons and weakened geomagnetic field intensity. We proposed that those resonant LWMAs induce the magnetic catalysis of iron oxides-silicate-like minerals (i.e., iron oxides, hyaline) from biogenic molecules and SARS-CoV-2 from endogenous viral elements in the genome, resulting in morbidity and mortality. The resultant SARS-CoV-2 particles are capable of replication within the host and transmission across hosts; however, SARS-CoV-2 infection per se does not induce morbidity or mortality in humans [98, 99]. Furthermore, we argue that the macrophage inflammatory response associated with COVID-19-morbidity and mortality is a foreign body-like reaction [100-102] to the magnetic catalysis-induced iron oxides-silicate-like minerals. Therefore, neither the SARS-CoV-2 infection nor the inflammatory reaction per se is the principal mediator of severe disease and mortality, which we termed, COVID-19. Indeed, children infected with SARS-CoV-2 have relatively higher viral loads, but reduced morbidity (and mortality) when compared to adults [103]. Furthermore, asymptomatic and symptomatic individuals with SARS-CoV-2 infection have a similar viral load [104]. Here, we investigated the presence of iron oxides-silicate-like minerals and SARS-CoV-2-like infection in the lungs and kidneys of laboratory rats, with an emerging severe acute respiratory disease and multiple thoracic organ pathology, in

the absence of experimental induction, and compared those pathologies to COVID-19 pathologies. We compared the ferromagnetic-like iron stores in COVID-19 high-risk and low-risk groups to determine the role of ferromagnetic-like iron-mediated magnetic catalysis in COVID-19-induced morbidity and mortality. Additionally, we investigated the relationship between the spatiotemporal dynamics of severe COVID-19 outbreaks, terrestrial water storage dynamics, and the lithospheric component of the geomagnetic field in tectonic plates with Proterozoic cratons to establish the role of serpentinization-induced LWMAs in mediating severe COVID-19 outbreaks. Furthermore, based on the predictions by Bility, M. T., 2019 [105], which posited the emergence of a geomagnetic field-driven, multi-year, oscillatory, severe acute respiratory syndrome epidemic in North America; we evaluated the clinical and temporal relationship between the vaping-associated severe acute respiratory syndrome epidemic of 2019 and the COVID-19 epidemic of 2020 in North America.

2. Materials and Methods

2.1 The Rat colony. Adult male and female immunodeficient Sprague Dawley rats (SRG rats), carrying mutations in the recombination activating gene 2 (RAG2) and interleukin-2 receptor subunit gamma (IL2Rγ) were obtained from the vendor (Hera BioLabs, Lexington, KY) and bred at the University of Pittsburgh beginning in July 2018. The rats were housed under specific-pathogen-free conditions in microisolator cages (generally 2 per cage, with an occasional single housing), on stainless steel (an iron alloy) racks (Model Number RS10147U40MVSPSHR-R, Allentown Caging Equipment Company, Allentown, NJ), fed irradiated chow and autoclaved water, and handled in a biosafety cabinet. The animals were housed in 12 hours light/12 hours dark cycle, (7 AM to 7 PM), with temperatures of 65-75°F

(~18-23°C) with 40-60% humidity. At any given time, the colony was/is predominately composed of 70% adolescents and adults (>2 months, and up to 12 months old). The COVID-19-like disease outbreak study was performed retrospectively; the colony was neither designed to record COVID-19-like disease in the rats or investigate the effect of the geomagnetic field on the rats. Therefore, animals were sacrificed immediately upon recording the COVID-19-like disease to relieve suffering per the Institutional Animal Care and Use Committee (IACUC) guidelines. The COVID-19-like disease was only recorded in adult rats (> 6 months old), and predominately affected one of two cage mates. We have not recorded any disease in neonatal and juveniles. Within the colony, some animals were used to construct humanized rats for unrelated studies. In those unrelated studies, de-identified human fetal tissues were obtained from the Magee-Women's Hospital of the University of Pittsburgh Medical Center (UPMC) via the University of Pittsburgh, Health Sciences Tissue Bank and transplanted into the immunodeficient rats. The use of de-identified human fetal tissues to construct humanized rodents was reviewed and approved by the University of Pittsburgh IRB Office. The use of de-identified human fetal tissues did not constitute human subjects research as defined under federal regulations [45 CFR 46.102(d or f) and 21 CFR 56.102(c), (e), and (l)]. The use of human fetal liver-derived hematopoietic stem cells was reviewed and approved by the Human Stem Cell Research Oversight (hSCRO) at the University of Pittsburgh. The use of a transgenic animal (immunodeficient rats) was reviewed and approved by the Institutional Biosafety Committee (IBC) at the University of Pittsburgh. All animal studies in the colony were reviewed and approved by the Institutional Animal Care and Use Committee at the University of Pittsburgh and were conducted following approved guidelines. Human fetal tissues for constructing humanized rodents were handled and processed under biosafety level 2

conditions. Male and female neonatal rodents were myoablated via gamma radiation using cesium-137 irradiator, with a dose of 500 rads. Myoablated male and female neonatal rats were transplanted with human $CD34^+$ hematopoietic stem cells (via retroorbital injection of 0.2X10^6 cells) and followed on two weeks later with autologous fetal-thymus and liver in the renal capsule. Some rats were transplanted as adults with human CD34+ hematopoietic stem cells (via retroorbital injection of 0.2X10^6 cells) and autologous human skin. The proportion of severe COVID-19 diseased adult rats that were not irradiated and those that were irradiated and transplanted was comparable to their proportion in the colony. Therefore, the transplantation procedure does not appear to affect the susceptibility to severe COVID-19-like disease. We acknowledge that future studies should include a rigorous design to assess the impact of various factors, especially low-dose gamma radiation, as it is well-established that low dose radiation can have a hormesis effect on disease outcomes.

2.2 Gross and In situ analysis of tissues. The gross analysis was performed using a camera, with animals either euthanized or anesthetized before photographing. Blood was collected via retroorbital exsanguination and mixed with 20 mM Ethylenediaminetetraacetic acid at a 1:1 ratio. Images of the blood clotting were taken immediately or after storage in an inverted position in 4-degree Celsius. Indicated tissue samples from the rodents were fixed with formalin and embedded in paraffin. Paraffin-embedded, fixed sections were stained with anti-SARS-CoV-1/2 Nucleocapsid antibody (ThermoFisher Scientific, Catalog # MA1-7404), anti-SARS-CoV-2 Spike S1 protein antibody (ProSciΨ, Catalog # 9083), DAPI (4,6-diamidino-2-phenylindole), hematoxylin and eosin (ThermoFisher Scientific), or Perls' Prussian Blue-Iron stain kit (Polysciences). The immunoreactivity of the antibodies was determined via incubation

with DAB substrate (MACH 2 Detection Kit, Biocare Medical) and counterstaining with hematoxylin. For fluorescence detection, slides were excited with ultraviolet light, and emissions were detected at 457 nm for DAPI (Blue), 528 nm (Green), and 616 nm (Red) using microscopy. Gross images of tissues were not manipulated beyond cropping the original image to show tissues of interest. *In situ* staining-images of tissues were not manipulated.

2.3 Geological and geophysical analysis. The bedrocks of the tectonic plates were demarcated and classified by Yan-Jie Tang et al., 2013 (Earth-Science Reviews, Volume 118, March 2013, Pages 45-68). The geomagnetic field (and secular variation) and component lithospheric magnetic field maps were generated by the GFZ German Research Centre for Geosciences and Chijioke M. Idoko et al., 2019, respectively, using CHAMP and Swarm magnetometry satellites data. The geomagnetic field (and secular variation) data can be obtained here: https://www.gfz-potsdam.de/en/section/geomagnetism/topics/sources-of-the-earths-magnetic-field/core-field/. The scoring of the Proterozoic-associated lithospheric magnetic anomalies and normalization to the local geomagnetic field intensity was performed semi-quantitively, using the total area covered with Proterozoic bedrocks and the relative lithospheric magnetic anomalies and geomagnetic field intensity in the region. The ionospheric-vertical total electron count in the northern hemisphere was determined by Parwani, M. et al, 2019 (Russian Journal of Earth Sciences, VOL. 19, ES1003, doi:10.2205/2018ES000644, 2019) using navigational satellites data. The terrestrial water storage anomaly data and map were generated from the GRACE-FO gravimetry satellites and the associated data analysis tool (JPL-NASA; https://grace.jpl.nasa.gov/data-analysis-tool and the GFZ German Research Centre for Geosciences; http://gravis.gfz-potsdam.de/land).

2.4 COVID-19 epidemiology. The COVID-19 epidemiology data and maps were compiled and generated by Our World in Data (https://ourworldindata.org/coronavirus), John Hopkins University (https://coronavirus.jhu.edu/map.html), Kaiser Family Foundation (Growing Data Underscore that Communities of Color are Being Harder Hit by COVID-19; Samantha Artiga, Kendal Orgera, Olivia Pham, and Bradley Corallo, Apr 21, 2020; https://www.kff.org/policy-watch/growing-data-underscore-communities-color-harder-hit-covid-19/), and the United States Centers for Disease Control (https://www.cdc.gov/covid-data-tracker/#mobility).

2.5 Population demographics analysis. The demographics data of the United States were compiled, analyzed, and published by the U.S. Census Bureau (The Black Population: 2010, 2010 Census Briefs, 2011; https://www.census.gov/history/www/reference/maps/).

2.6 Social distancing and mask usage analysis. Social distancing was determined by the Center for Disease Control using transit, workplace, retail-recreational activities data collected by Google Mobility Reports, Safegraph Social Distancing Metrics, Cuebiq Mobility Insights (https://www.cdc.gov/covid-data-tracker/#mobility). Data and maps on mask usage (based on survey responses) were obtained from the Institute for Health Metrics and Evaluation at the University of Washington (http://covid19.healthdata.org/united-states-of-america/california?view=total-deaths&tab=trend). The data sources are the University of Maryland Social Data Science Center; Kaiser Family Foundation; YouGov COVID-19 Behaviour Tracker survey.

2.7 Air pollution analysis. The population-weighted average level of exposure to concentrations of suspended particles measuring less than 2.5 microns in diameter for the

world was obtained by The World Bank (World Development Indicators) for 1990-2016 and analyzed and published by the Our World In Data (https://ourworldindata.org/grapher/pm25-air-pollution). The data source is Brauer, M. et al. 2016, for the Global Burden of Disease Study 2016. The data is the estimated global population-weighted mean concentrations of particle mass with an aerodynamic diameter less than 2·5 μm (PM2·5) and ozone at an approximate 11 km × 11 km resolution based on satellite-based estimates, chemical transport models, and ground-level measurements.

2.8 Climate analysis. The Köppen-Geiger-Photovoltaic (PV) climate classification with the 12 most relevant climate zones across the world was analyzed and classified by JuliánAscencio-Vásquez et al. The map was published in Solar Energy Volume 191, October 2019, Pages 672-685 (Methodology of Köppen-Geiger-Photovoltaic climate classification and implications to worldwide mapping of PV system performance). The global climate classification and global PV performance modeling were developed using satellite-based estimates and ground-level measurements for ambient temperature, precipitation, and irradiation.

3. Results

3.1 The unrecognized role of serpentinization-induced aberrant lithospheric long-wavelength magnetic anomalies in mediating COVID-19 via magnetic catalysis

It is well established that geological and geophysical forces maintain the carbonate–silicate geochemical cycle [106-108]. We propose that the serpentinization of peridotites in the lithospheric mantle via interaction with carbon dioxide-enriched water results in the generation of LWMAs in tectonic plates with Precambrian cratons during conditions in the Holocene with

increased atmospheric carbon dioxide and terrestrial water storage and severely weakened geomagnetic field intensity [21, 109-111]. Specifically, the production of ferromagnetic-like (ferrimagnetic) iron oxides-silicate rock minerals via serpentinization [21, 112] results in the generation of LWMAs, which are influenced by the interplanetary magnetic field (heliospheric magnetic field) in a weakened geomagnetic field [25]. This serpentinization of peridotites during geologic conditions with excess atmospheric carbon dioxide levels enables sequestration of the excess atmospheric carbon dioxide into lithospheric rock minerals [22, 106, 108]. We hypothesize that COVID-19 pathologies in humans and animals result from the aberrant transformation of tissues (chiral biomolecules), metals, gases, and endogenous viral elements in the human genome via resonant LWMAs-induced magnetic catalysis. The LWMAs (waveband >100 kilometers and up to 5000 kilometers) that mediate the SARS-CoV-2-associated COVID-19 pathologies are

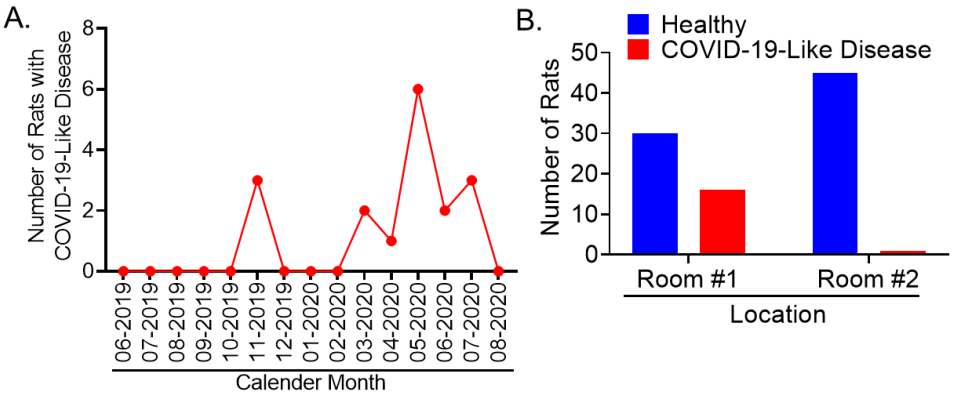

Figure 1: The spatiotemporal dynamics of COVID-19-like disease in laboratory rats in the absence of experimental induction. We recorded COVID-19-like symptoms (namely, labored/difficulty breathing and hemorrhaging-blood around nose) in laboratory rats via syndromic surveillance that included three times per day visual monitoring. (A) The values denote the total numbers of rats that developed COVID-19-like symptoms in a given month. (B) the values denote the total number of rats that developed COVID-19-like disease and the total number of rats that did not developed disease (healthy) for a given room location. The fisher's exact test P value = <0.0001. The result is significant at $p < .05$. Upon recording the COVID-19-like disease, the rats were immediately sacrificed (per humane research guildelines) and the COVID-19-like pathologies in the thoracic organs were confirmed via necropsy. The rat colony was not designed beforehand to study COVID-19-like disease, and the syndromic surveillance procedures were instituted as a general welfare check to insure a healthy colony. The rats were housed at approximately equal ratio in two adjacent rooms. The total number of rats observed in the study period was ~ 92 and ~46 per sex. The COVID-19-like disease was recorded predominately in one room. Animals were handled by the same staff (in biosafety level 2 personal protective equipment). The rats were house in autoclaved microisolator cages on steel (iron alloy) racks, and always handled in a biosafety cabinet-Class 2, provided autoclaved bedding and water, and sterilized food.

generated in the lithospheric mantle of tectonic plates with Proterozoic cratons, during serpentinization-mediated production of iron oxides-silicate rock minerals [21, 22, 109, 113, 114]. Consistent with this hypothesis, the formation of Proterozoic bedrocks in the Precambrian eon was associated with the Great Oxidation Event and orogenic activity that resulted in the formation of significant iron oxides-silicate rock minerals deposits in the lithosphere [115-117]. In support of this hypothesis, evidence in genomics demonstrates the presence of endogenous forms of human viruses, including the so-called emerging viruses, in the genome of humans and many terrestrial animals (including bats) [95-97, 118, 119]. Evidence also demonstrate critical roles for endogenous viral genes in normal development and physiology, suggesting that the manifestation of viruses in pathologic conditions could be a result of an aberrant transformation of endogenous viral elements [120]. It is well-established that chemical (including biochemical) reactions are spin restricted [57, 60]. Consequently, altering the spin of reactants in a chemical reaction via an external magnetic field result in altered rates of reaction and altered products, termed magnetic catalysis [121-125]. Magnetic catalysis overcomes the mass-isotope restriction of chemical reactions [49, 60, 121-125]. Recent advances also demonstrate that the application of ferromagnetic material-derived electrons to chiral biomolecules, such as double-stranded deoxyribonucleic acid (dsDNA) results in the efficient generation of spin-polarized currents, and termed the chiral-induced spin selectivity (CISS) effect [57, 58, 126-134]. Additionally, A.

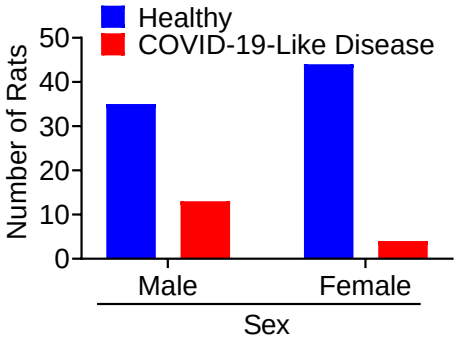

Figure 2: The sex differences in COVID-19-like disease in a laboratory rats in the absence of experimental induction. We recorded the COVID-19-like symptoms (namely, labored difficulty breathing and hemorrhaging-blood around nose) predominately in male (M) rats (13 of 46 males), compared to female (F) rats (4 of 46 females) despite approximately equal number of both sexes in the colony. The fisher's exact test P value = 0.03. The result is significant at $p < .05$.

L. Buchachenko et al. have demonstrated that magnetic isotope and magnetic field effects modulate DNA synthesis [135]. These developments suggest that interaction of chiral biomolecules (such as dsDNA of endogenous viruses, lipids, carbohydrates, and proteins) on ferromagnetic-like (superparamagnetic) minerals with resonant LWMAs could result in the magnetic catalysis of aberrant molecules and replication-competent, transmissible

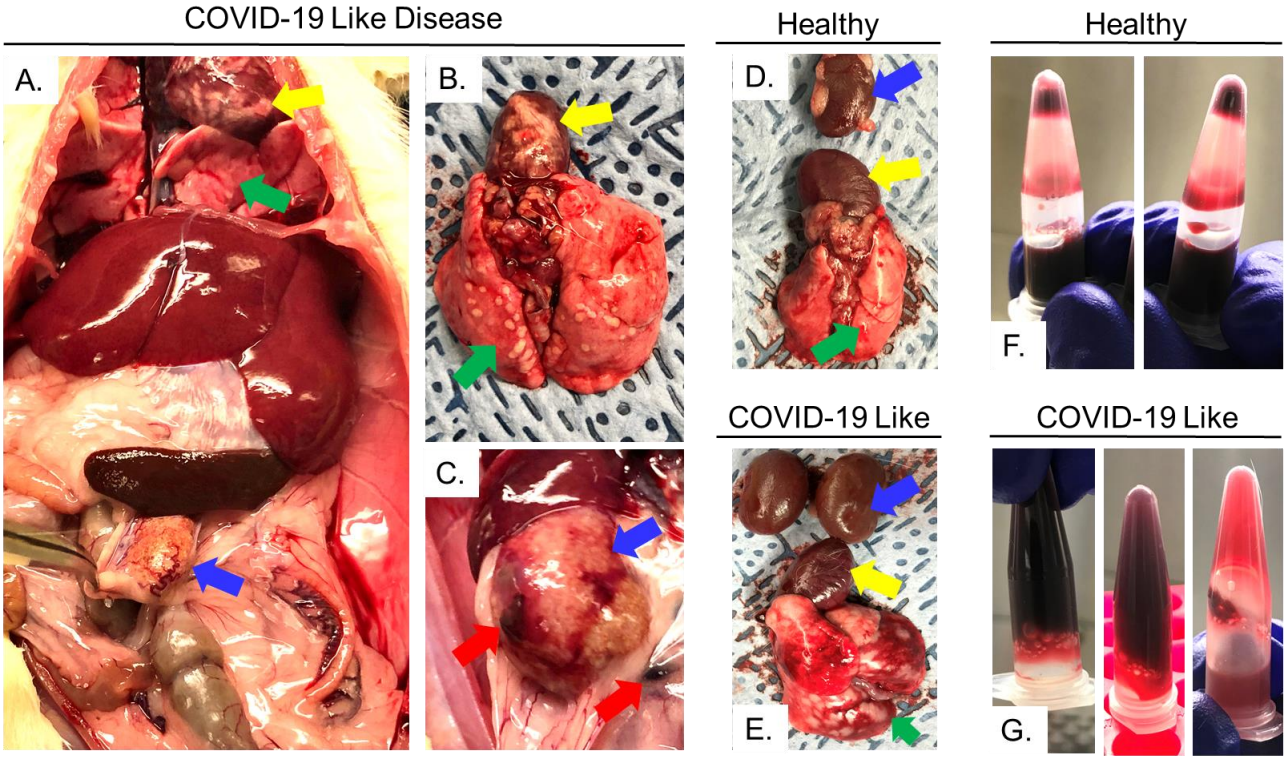

Figure 3: Gross pathology of a COVID-19-like disease in a laboratory rats in the absence of experimental induction. Representative gross analysis of lung (green arrow), heart (yellow arrow) and kidney (blue arrow) in a COVID-19-like diseased (n=17) rats demonstrates the presence thoracic organs damage (A), with lung and heart (B), and kidney (C) pathologies, including blood clots (red) highlighted. (D) Representative gross analysis of lung (green arrow), heart (yellow arrow) and kidney (blue arrow) in a healthy rat demonstrates the absence of lung, heart, and kidney pathology. (E) Representative gross analysis of lung (green arrow), heart (yellow arrow) and kidney (blue arrow) in a COVID-19-like diseased rat demonstrates the severe lung with hemorrhagic pathology, albeit the kidney and heart in this animal appear normal. Gross lung damage was recorded in 100% of the necropsy, while both gross lung and kidney damage was recorded in ~ 50% of the cases. Gross damage to the heart was recorded in a single animal. (F) Analysis of the blood (diluted at 1:1 using 20mM EDTA-anticoagulant) from a healthy rat demonstrates a lack of viscosity, with the blood flowing to the bottom of the tube after ~10 seconds following withdrawal. (G) On the contrary, analysis of the blood (also diluted at 1:1 using 20mM EDTA-anticoagulant) from a COVID-19-like diseased rat, demonstrates severe viscosity (viscous clot), with the blood unable to flow to the bottom of the tube after ~10 seconds, following withdrawal (G-Left panel) and ~10 minutes following storage at 4 degree Celsius in an inverted position (G-Middle panel); dilution of the blood at 1:10 using 20mM EDTA-anticoagulant further demonstrates that the blood immediately clots in less than 10 seconds, with the viscous clot lodged on the side of the tube (G-Right panel). Blood coagulation was recorded in ~50% of the COVID-19-like cases.

biomolecules, such as SARS-CoV-2 particles [57, 58, 136, 137]. Here, we proposed that serpentinization-induced resonant LWMAs interacts with ferromagnetic-like iron stores (i.e., ferrihydrite) in the host, and subsequently interacts with ferrous iron (Fe^{2+}) and dioxygen (O_2) in hemoglobin in red blood cells, to catalyze ferric iron (Fe^{3+}) formation, and subsequently catalyze iron oxides formation via interaction with water molecules (H_2O) in the blood, like during serpentinization [23, 112, 138]. This magnetic catalysis of iron oxides in red blood cells

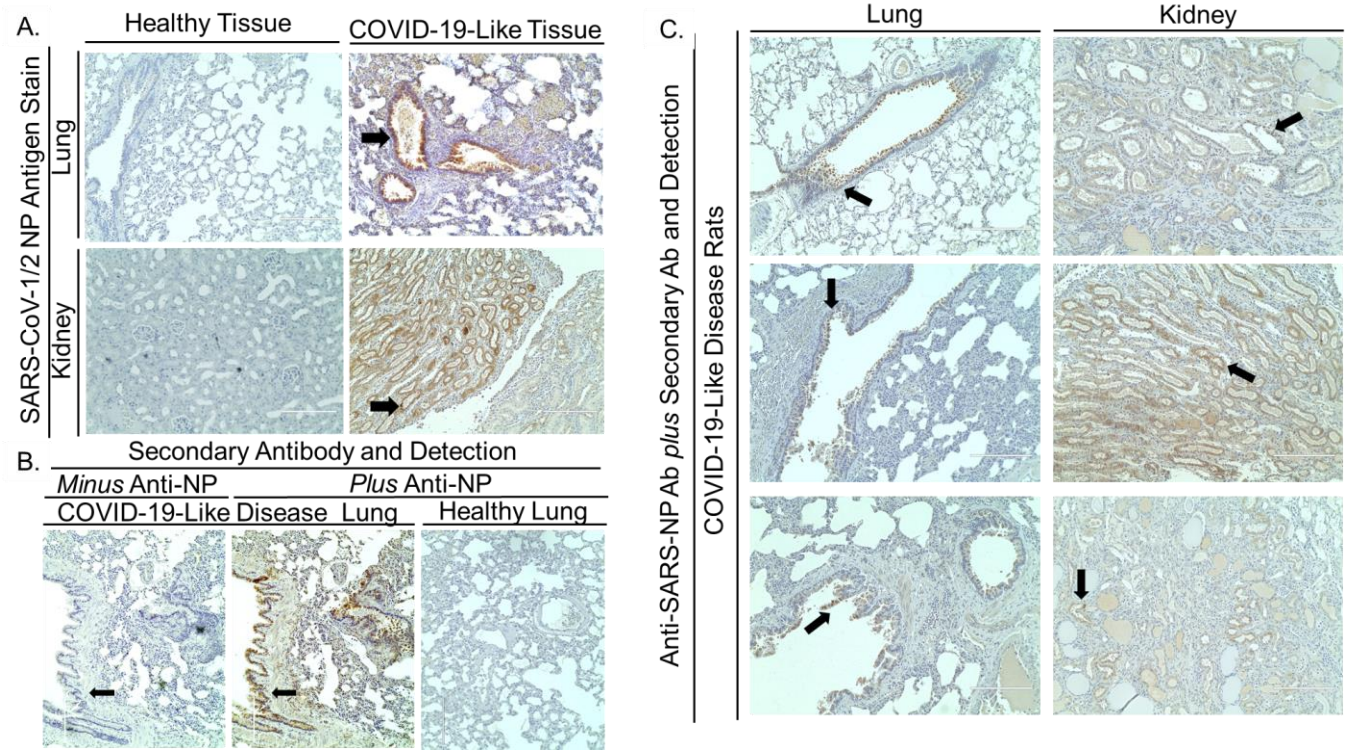

Figure 4: SARS-CoV-2-like Nucleocapsid antigen in COVID-19-like diseased laboratory rats in the absence of experimental induction. (A) Immunohistochemistry analysis of SARS-CoV-1/2 nucleocapsid (brown) in healthy (column 1) and COVID-19-like diseased rats (n=3, from November 2019, column 3) demonstrate the presence of the SARS-CoV-1/2 Nucleocapsid antigen in the lung epithelial cells and renal tubular epithelial cells in COVID-19-like diseased rats (black arrow). (B) Immunohistochemistry staining of the lung from COVID-19-like diseased rat (from November 2019, column 1-2) with the detection system (secondary antibody and the chromogen detector) in the absence (column 1, *Minus Anti-NP*) or presence (column 2, *Plus Anti-NP*) of anti-SARS-CoV-1/2 nucleocapsid primary antibody (brown) demostrates the specificity of the staining procedure. The staining of the lung from a healthy rat (column 3) with anti-SARS-CoV-1/2 nucleocapsid primary antibody and the detection system (secondary antibody and the chromogen detector) confirms the specificity of the staining procedure. (C) Immunohistochemistry analysis of SARS-CoV-1/2 nucleocapsid (brown) in COVID-19-like diseased rats (n=5, from March-July 2020) demonstrate the presence of the SARS-CoV-1/2 Nucleocapsid antigen in the lung epithelial cells and renal tubular epithelial cells in COVID-19-like diseased rats (black arrow). Note: Molecular diagnostics for SARS-CoV-2 antigen was not perform on all animals with the COVID-19-like disease. The specificity of the anti-SARS-CoV-1/2 nucleocapsid primary antibody was validated by Alejandro Best Rocha et al, 2020 in human samples.

in COVID-19 results in a rapid depletion of bioavailable dioxygen (anoxic condition) and water molecules (dehydration) [112]. Furth ermore, those iron oxides minerals (i.e., black particles) in the red blood cells are ferromagnetic-like (superparamagnetic); thus, the red blood cells form a gelatinous-like substance (viscous blood clots)[139] in the dehydrated blood in vessels,

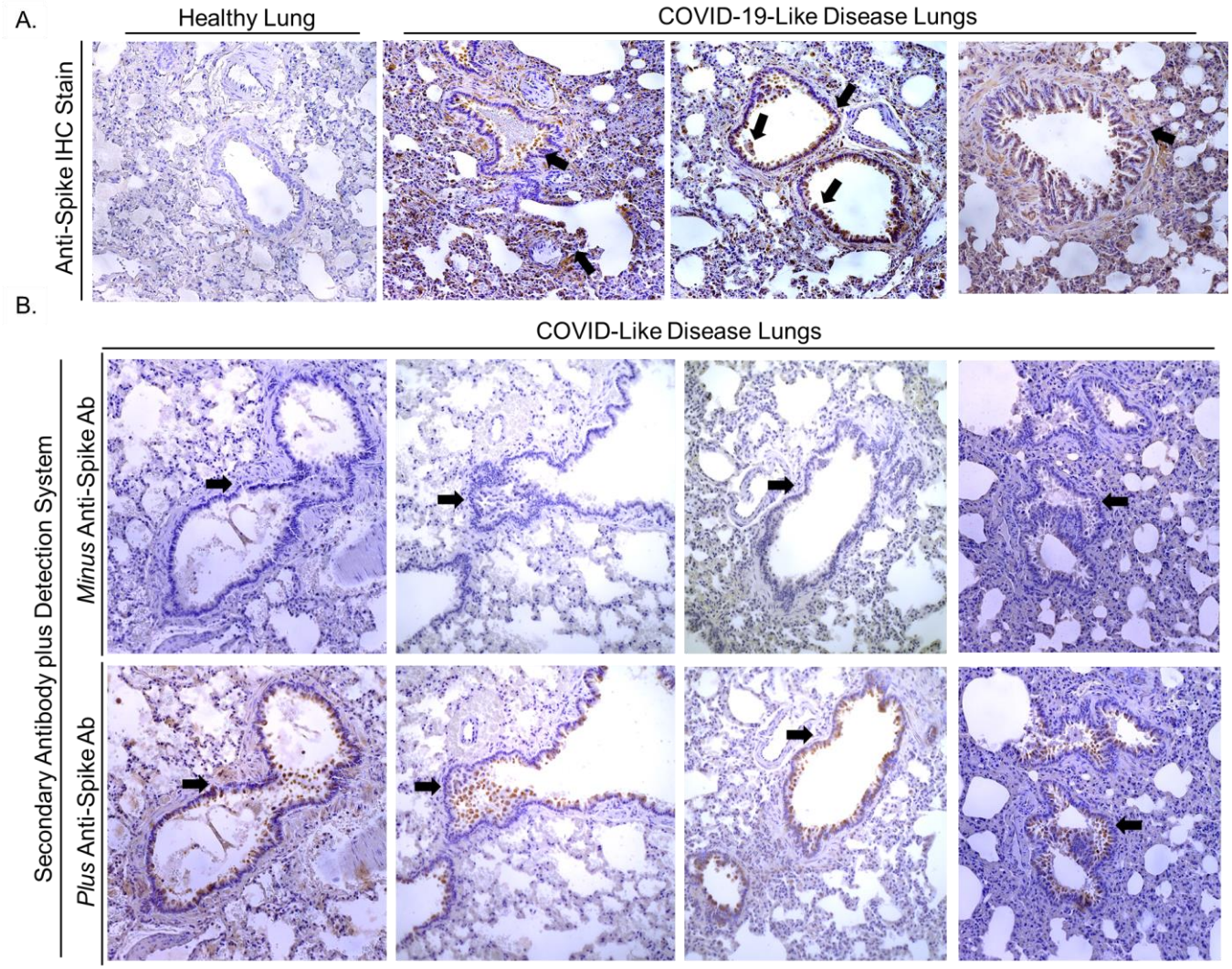

Figure 5: SARS-CoV-2-like Spike antigen in COVID-19-like diseased laboratory rats in the absence of experimental induction. (A) Immunohistochemistry analysis of SARS-CoV-2 Spike protein (brown) in healthy (column 1) and COVID-19-like diseased rats (n=4, from March-July 2020, column 2-4) demonstrate the presence of the SARS-CoV-2 Spike antigen in the lung epithelial cells in COVID-19-like diseased rats (black arrow). (B) Immunohistochemistry staining of the lung from COVID-19-like diseased rat (n=4, from March-July 2020) with the detection system (secondary antibody and the chromogen detector) in the absence (row 1, *Minus Anti-Spike*) or presence (row 2, *Plus Anti-Spike*) of anti-SARS-CoV-2 Spike protein primary antibody (brown) demostrates the specificity of the staining procedure. Note: Molecular diagnostics for SARS-CoV-2 antigen was not perform on all animals with the COVID-19-like disease. The specificity of the anti-SARS-CoV-2 Spike protein primary antibody was validated by the vendor in human samples (the data is available at https://www.prosci-inc.com/sars-cov-2-covid-19-spike-s1-antibody-9083.html)

cavities, and tissues (i.e., lung, kidney) [140]. Here, we propose that serpentinization-induced resonant LWMA- ferromagnetic-like iron oxides (and iron oxyhydroxide) interactions also mediate the magnetic catalysis of ferromagnesian silicate-like minerals from biogenic molecules [23, 138, 141, 142].

Over the past nine months, we recorded a COVID-19-like, severe acute respiratory syndrome disease (in 17 per ~92 rats (~18%), with 76% males and 24% females) in adult laboratory rats (all diseased animals were >6 months old) Pittsburgh, Pennsylvania, which temporally overlaps with the emergence of severe acute respiratory diseases in humans in the Northeastern United States **(Figure 1, 2**). The rat colony had an approximately equal number

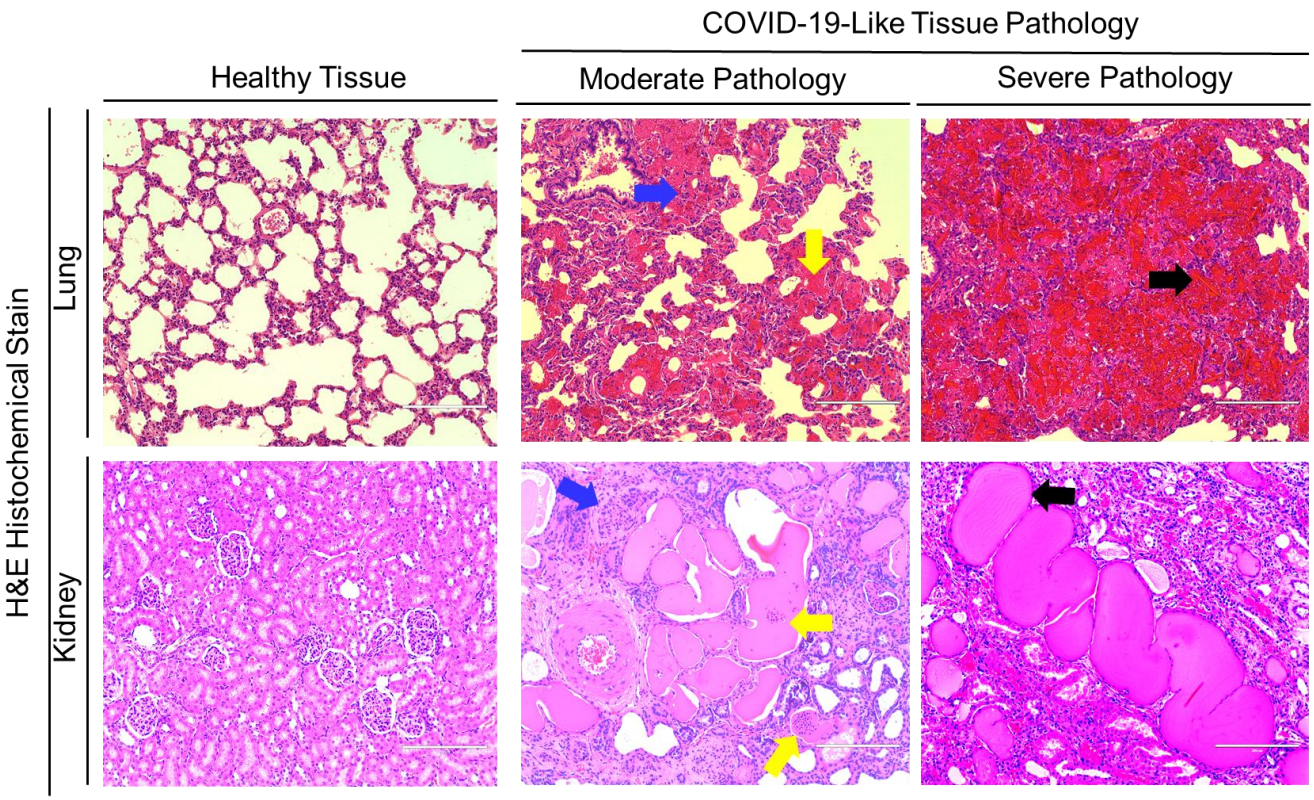

Figure 6: COVID-19-like tissue pathology in the theoracic organs of laboratory rats in the absence of experimental induction. Histopathological (Hematoxylin and Eosin stain) analysis of lung (row 1) and kidney (row 2) tissues in healthy and COVID-19-like diseased (n=8) rats demonstrates the presence lung and kidney pathology, including inflammation and giant cells formation (blue arrow, column 4), and hyaline structures (yellow arrow, column 2), which progresses severe pathology, including hemorrhaging and silicate-like minerals (black arrow, column 3).

of male and female immunodeficient Recombination activating gene-2 protein and interleukin-2 receptor subunit gamma double knockout-Sprague Dawley rats and had been maintained continuously since July 2018 (*see details in method section*). The COVID-19-like disease disproportionally affected males, which recapitulates the COVID-19-induced morbidity and mortality in humans (**Figure 2**). The COVID-19-like disease in the rats occurred rapidly, with rats exhibiting excellent health status (normal movement, breathing, eating, and drinking) in the prior evening, but incapable of breathing and hemorrhaging (and seizure in one case) by

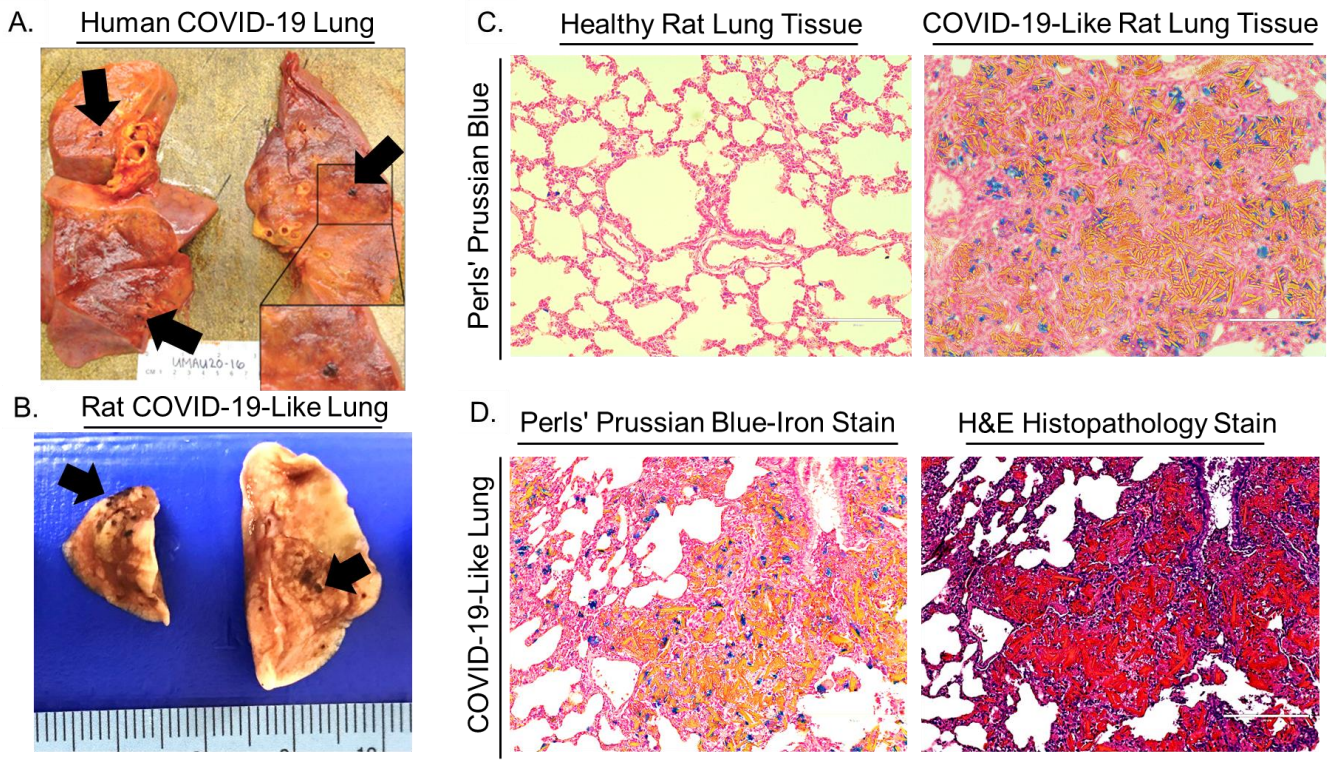

Figure 7: The co-localization of ferromagnetic-like iron and serpentinization-like mineralization in the lung of COVID-19-like diseased laboratory rat in the absence of experimental induction. (A) Gross analysis of COVID-19 lungs in humans by Sharon E. Fox et al, 2020, demonstrates the presence of hardened tan-grey consolidations and dark-colored hemorrhagic patches with focal demarcation. (A) Gross analysis of COVID-19-like lungs in rats recapitulates the presence of hardened tan-grey consolidations and dark-colored hemorrhagic patches with focal demarcation. Note: The rat lung was fixed in formalin. (C) Tissue iron analysis (Perls' Prussian blue staining) in the lungs of laboratory rats with COVID-19-like disease demonstrates the presence of crystal (silicate-like) structures, which co-localized with iron oxides (golden brown/rust-like; right panel) and ferric iron (Fe^{3+}) (blue stain-right panel); these features were absent in health-control tissue (left panel). (D) These iron oxides-silicate-like structures co-localized with severe hemorrhaging (Bright red color in H&E stain). Note: The representative tissues shown here were obtained from COVID-19 diseased immunodeficient rats that were previously irradiated or transplanted with human hematopoietic-lineage cells and thymic-lymphoid tissue (~6 months prior to onset of disease).

the next morning. Gross, histological, and immunohistochemistry analysis of the major organs in the COVID-19-like diseased rats demonstrate significant blood clotting, hardened tan gray/pale patches, and black-hemorrhagic patches in the lungs and kidneys, along with silicate/glass-like structures, and the presence of SARS-CoV-2-like antigens in the lung and

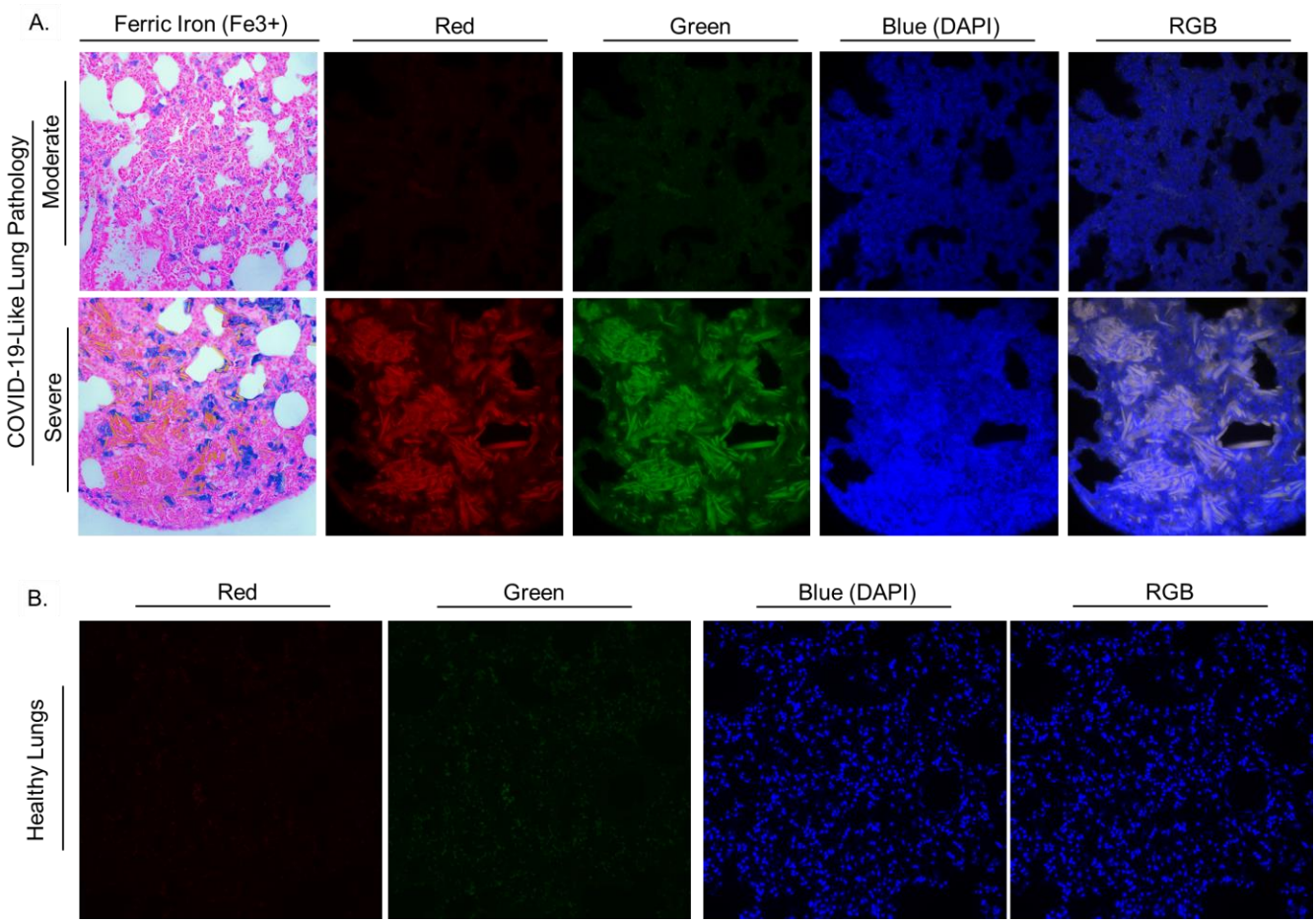

Figure 8: Fluorescent ferromagnesian silicate-like minerals in the lung of COVID-19-like diseased laboratory rat in the absence of experimental induction. (A) Analysis of serial lung tissue sections from a rat with COVID-19-like disease demonstrates the presence of silicate-like (serpentine-like) structures, which co-localized with iron oxides (golden brown/rust-like; column 1, bottom row) and ferric iron (Fe^{3+}) (blue stain-column 1, bottom row). The ferromagnesian silicate-like (serpentine-like) mineral emit red (Fe^{3+} in iron oxide) and green (Fe^{3+} in serpentine) fluorescence upon excitation with ultraviolet light (column 2-5, bottom row), with the composite signal whitish. Analysis of a lung tissue region with moderate pathology in the same animal, demonstrates low level of ferric iron (blue stain-column 1, top row) and negligible levels of iron oxides-silicate-like minerals (golden brown/rust-like; column 1, top row). Both tissue regions emit blue flourescenece due to DAPI (4,6-diamidino-2-phenylindole) staining of deoxyribonucleic acid (DNA), with marginal levels of blue fluorescence emitted by the ferromagnesian silicate-like (serpentine-like) minerals. (B) Analysis of a lung tissue from a healthy rat demonstrate the absence of fluorescent ferromagnesian-silicate like minerals, thus confirming the specificity of the red and green fluorescent signals in the COVID-19-like diseased lung. The healthy lung tissue emit blue flourescenece due to DAPI staining of the DNA. RGB denotes the composite image of the Red, Green and Blue signals.

kidney epithelium (**Figure 3, 4, 5, 6**), which recapitulates COVID-19 pathology and the associated SARS-CoV-2 infection in humans [55, 139, 143-148]. The silicate/glass-like structures in the lungs and kidneys of the COVID-19-like diseased rats mimic the various stages associated with serpentinization-mediated rock mineralization (**Figure 7**) [112]. Tissue iron analysis in the lung of a COVID-19-like diseased rat demonstrates the presence of ferric iron (Fe 3+) and iron oxides (golden brown/rust-like) particles coupled with the silicate/glass-like structures and patches with hemorrhagic infiltrates (**Figure 7**). The silicate/glass-like structures and iron oxides deposits in the lungs and kidneys of the COVID-19-like diseased rat are consistent with tissue pathologies in COVID-19-induced mortality [50, 51]. Additionally, the ferromagnesian silicate-like minerals in the COVID-19-like diseased lung predominately emit red (Fe3+ in iron oxide minerals) and green (Fe3+ in serpentine) fluorescence upon excitation with ultraviolet light, and a composite whitish color (**Figure 8**), which is consistent with the fluorescent properties of serpentinization-induced rock minerals [149].

3.2 Abnormally high ferromagnetic-like iron stores (hyperferritinemia) in humans is the unifying determinant of COVID-19 morbidity and mortality

In the proposed hypothesis, ferromagnetic-like/superparamagnetic iron stores (i.e., ferrihydrite) in humans [150] is critical for resonant LWMA-mediated magnetic catalysis in COVID-19 pathologies. Iron stores are low in children and increases with age, with the highest levels in the elderly [151-155]. Males have significantly higher iron stores compared to females [156]. Consequently, COVID-19-induced morbidity and mortality risk are directly proportional to age [157-159], and male sex is also a significant risk factor for COVID-19-induced morbidity and mortality [157]. Individuals with metabolic syndrome (obesity [160-162], diabetes [163-165],

and cardiovascular disease [166-168]) have higher COVID-19-induced morbidity and mortality due to abnormally high iron stores compared to matched-healthy individuals. Several studies have demonstrated that COVID-19 patients exhibit abnormally high iron stores (using serum ferritin levels [169, 170] as a surrogate marker) [171, 172], and a retrospective, multicenter

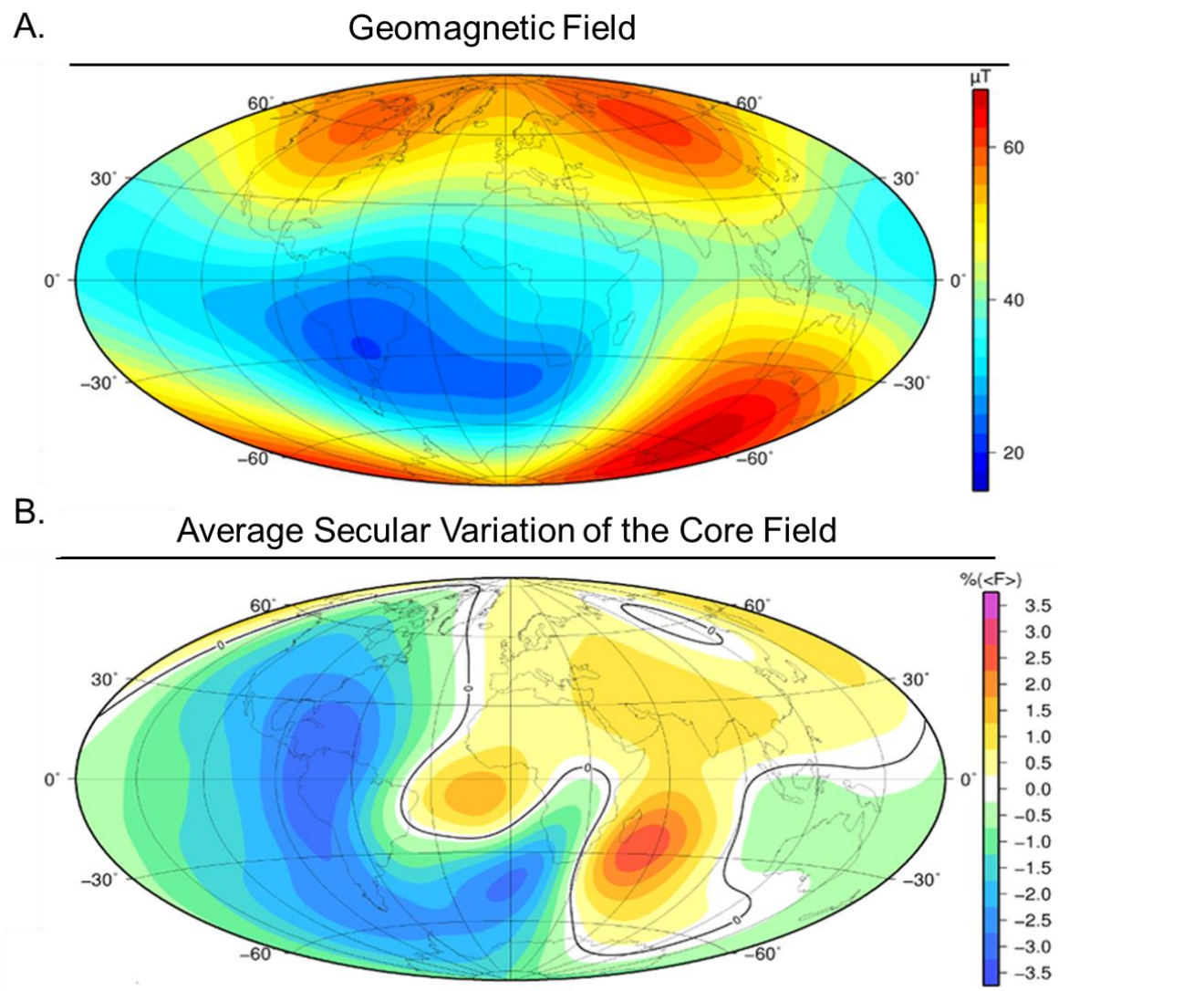

Figure 9: Continental regions with weakening geomagnetic field intensity have severe COVID-19 outbreaks. The geomagnetic field intensity (A) and secular variation (B) as determined by ESA's CHAMP and Swarm magnetometry satellites by the GFZ German Research Centre for Geosciences. (A) The intensity of the total field is highest in the Polar Regions and lowest in the South Atlantic anomaly. (B) The secular variation of the core field from 2006-2016 demonstrates a weakening geomagnetic field intensity. The most severe weakening in the geomagnetic field intensity is occurring on the North and South American tectonic plates (and the southern tip of Africa) and those regions are experiencing severe COVID-19 outbreaks. The basins in Western Eurasia (Europe) also experience weakening geomagnetic field ossilations, with the strengthening field intensity in the Eurasian plate predominately occuring in Eastern Eurasia (Asia). COVID-19 outbreaks have been more severe in Western Eurasia (Europe) than Eastern Eurasia (Asia). The geomagnetic field in the African plate has also been strengthening.

cohort study of hospitalized COVID-19 patients confirmed that abnormally high iron stores constitute a significant determinant of COVID-19-induced mortality [172-175]

3.3 The relationship between the spatial dynamics of severe COVID-19 outbreaks and the lithospheric component of the geomagnetic field

The geomagnetic field is a coupled magnetic field [25, 176-178]. It consists of the core, mantle, lithospheric, ionospheric, and magnetospheric magnetic fields (demarcated based on spherical harmonics modeling), which are further coupled to the interplanetary magnetic field (the heliospheric magnetic field) [25, 176-178]. The geomagnetic field intensity is highest in the Polar Regions and lowest in the equatorial region (especially in the South Atlantic Anomaly) (**Figure 9**). The total geomagnetic field intensity has been weakening over the past millennium, with the North and South American plates (and the southern tip of the African plate) experiencing the most severe weakening (**Figure 9**). On the contrary, the eastern portion of the Eurasian plate-Asia and the Africa plate (excluding the southern tip of Africa) have experienced a relative strengthening of the geomagnetic field intensity (**Figure 9**). Additionally, the intensity of the lithospheric component of the geomagnetic field has been increasing in regions with Precambrian cratons, with regions on the North and South American plates with Proterozoic-Precambrian cratons exhibiting the highest increase [179]. Here, we examine the relationship between the lithospheric component of this weakening geomagnetic field and the SARS-CoV-2-associated COVID-19 pandemic. A severe, locally-restricted COVID-19 outbreak was first recorded on the Yangtze craton (in Wuhan and surrounding cities) [180] in the eastern portion of the Eurasian plate. The subsequent severe outbreaks spread westerly

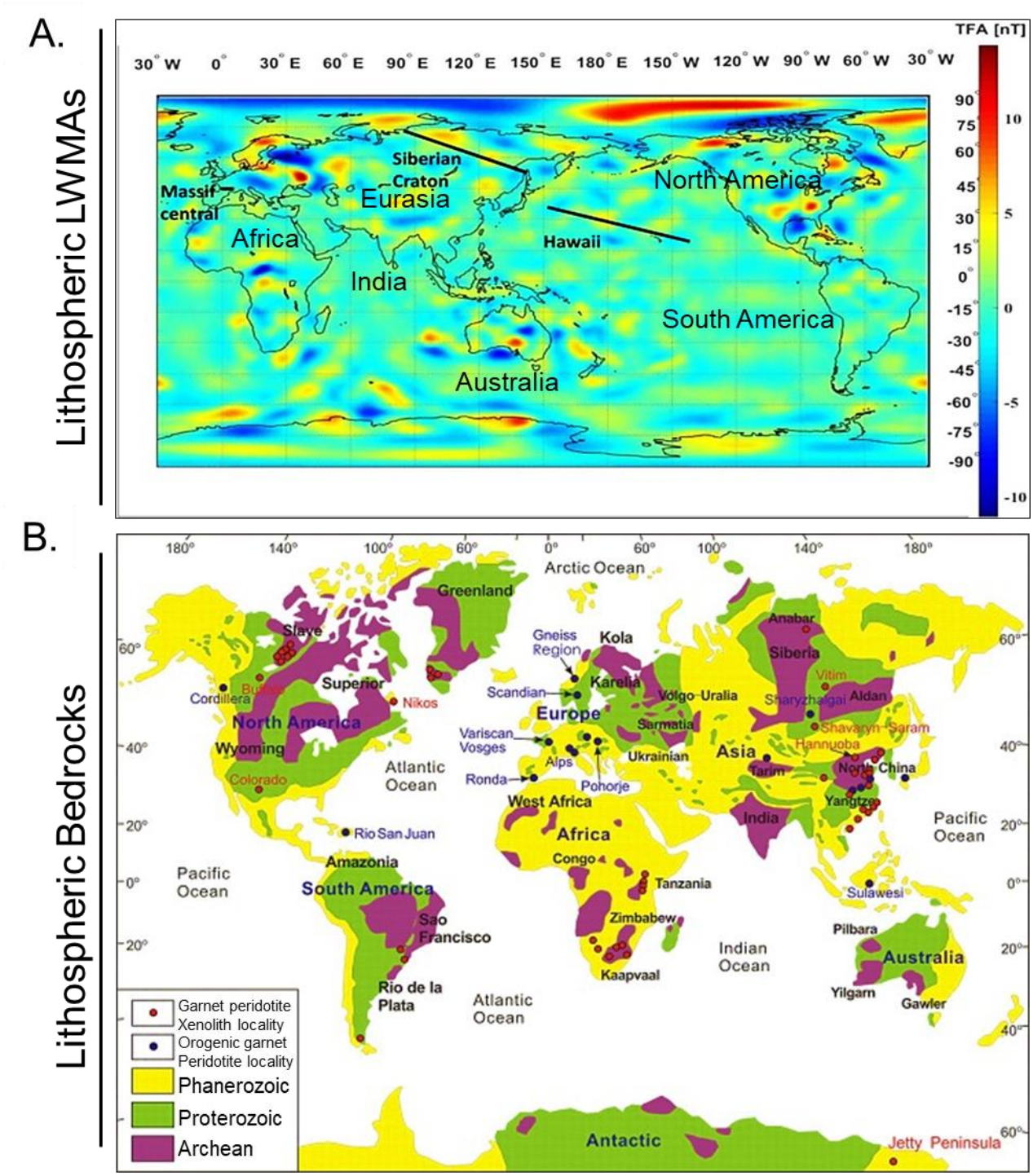

Figure 10: Severe COVID-19 outbreaks are/will be restricted to tectonic plates with long-wavelength magnetic anomalies in Proterozoic cratons. Severe COVID-19 outbreaks have predominately occurred in the western portion of the Eurasian plate and the American plates. Geophysical and geological analysis by Chijioke M. Idoko et al, 2019 and Yan-Jie Tang et al, 2013, respectively, demonstrate that Proterozoic cratons in the North American, Eurasian (especially in the western portion-Europe), and South American tectonic plates are associated with lithospheric long-wavelength magnetic anomalies. The LWMAs in the African and Australian plates are associated with Archean cratons, while the LWMAs in the Indian plate are associated with the collision zone with the Eurasian plate. The Arabian plate has marginal LWMAs, albiet it is in collision with the Euraian plate.

on the Eurasian plate along the Greater Tethyan Eurasian orogenic belt (the Alpine-Himalayan orogenic belt [181-186]) and subsequently along the Appalachian-Ouachita orogenic belt on the North American plate and to the South American tectonic plate. Severe COVID-19 outbreaks predominately co-localize with the troughs of the lithospheric LWMAs [109] in tectonic plates with Proterozoic cratons, which are basin regions with population centers

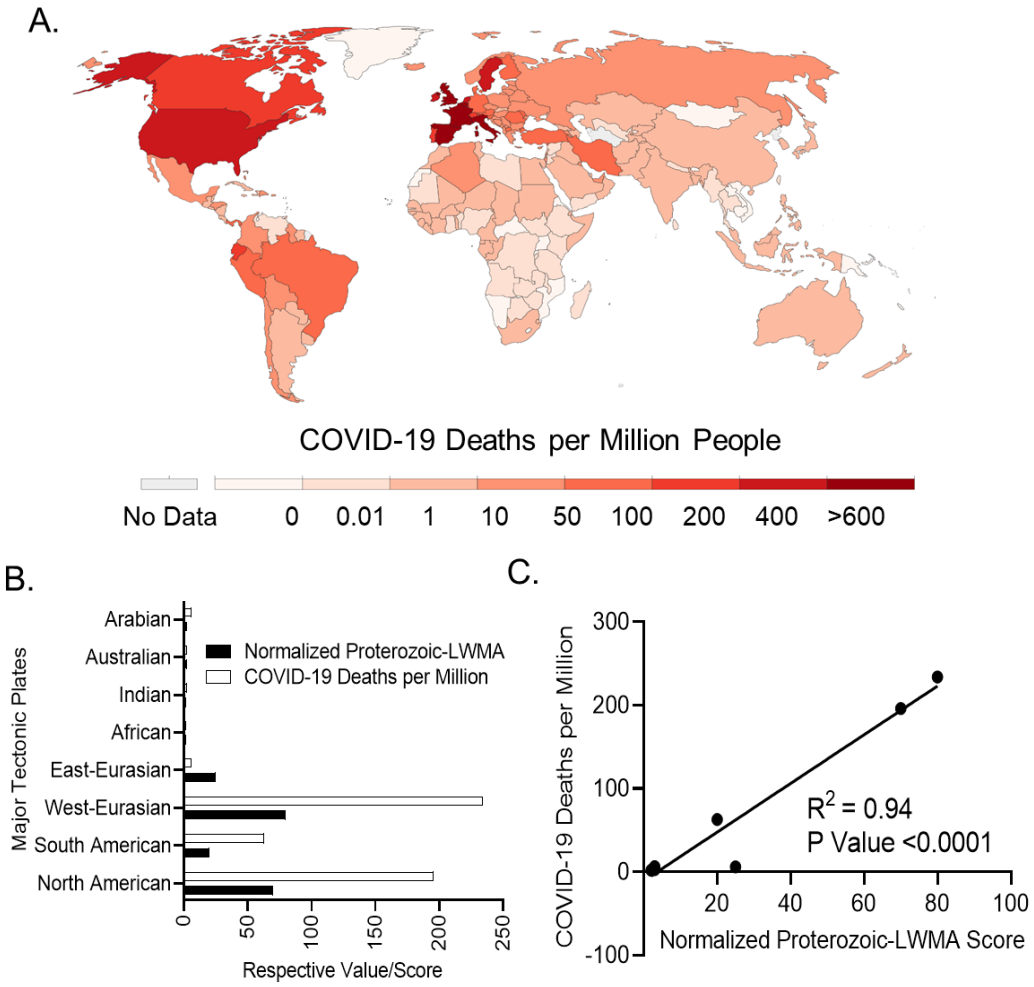

Figure 11: Severity of COVID-19 outbreaks in the tectonic plates is associated with the intensity of long-wavelength magnetic anomalies in Proterozoic cratons in a weakened geomagnetic field. (A) Analysis of epidemiological data by Change Data Lab (May 21, 2020) demonstrates that countries on the North American, Western Eurasia-Europe, and South American tectonic plates are associated with higher COVID-19 deaths per million people. (B) Analysis of the intensity of Proterozoic bedrock-associated LWMAs normalized to the intensity of the total geomagnetic field (semi-quantitative score: area covered and relative intensity) in the major tectonic plates and the severity of COVID-19 outbreaks (Derived from John Hopkins University-Coronavirus Center, ending on May 21, 2020) on those tectonic plates (C) demonstrates a direct association. The values for the LWMAs score denotes a single value of the entire plate. The values for the deaths per million on the tectonic plate denotes the total recorded COVID-19 deaths divided by the total human population on the plate.

(**Figure 10**). Severe outbreaks spread from the Yangtze River basin (Eastern Eurasia) to basins in Central Eurasia (Iran), Western Eurasia, the eastern portion of the North American plate, and subsequently to the basins on the South American plate [187]. The Greater Tethyan Eurasian orogenic belt has active serpentinization of peridotites and significant lithospheric LWMAs (**Figure 10**) [109, 181, 185, 188]. The Appalachian-Ouachita orogenic belt also has active serpentinization of peridotites and significant lithospheric LWMAs (**Figure 10**) [189-191]. The pandemic also spread easterly, albeit less severe outbreaks in basins on the Korean Peninsula, the Island of Japan, and the western portion of the North America plate (**Figure 10**). Consistent with this bi-directional (westerly and easterly) spread of COVID-19 outbreaks from the Yangtze craton [192], the predominant SARS-CoV-2 strain in the eastern portion of the North American plate during the vernal period of the pandemic is genetically similar to the predominant strain in the western portion of the Eurasian plate, while the predominant coronavirus strain in the western portion of the North American plate is genetically similar to the predominant strain in the eastern portion of the Eurasian plate; even though travel between Eurasia and North America is a fraction of the travel within North America [193]. Additionally, the severity of COVID-19 outbreaks on the North American and Eurasian tectonic plates during the vernal phase of the pandemic is directly proportional to the intensity of the Proterozoic cratons-associated LWMAs (**Figure 11**) [109, 114]. Tectonic plates with marginal Proterozoic cratons-associated LWMAs (the African, Arabian, Indian, and Australian plates) will experience relatively less severe COVID-19 outbreaks (**Figure 11**) [109, 114]; especially in continental regions farthest away from the collision zones with the Eurasian plate (i.e., Sub-Saharan Africa). Furthermore, the governing hydromagnetic perturbations and the South Atlantic

Anomaly that are driving the weakening geomagnetic field intensity are predominately restricted to Eurasia and the Americas (and the southern tip of Africa) [9].

3.4 The relationship between the temporal dynamics of severe COVID-19 outbreaks and the lithospheric component of the geomagnetic field dynamics

Severe COVID-19 outbreaks were first recorded in Eurasia in the early months (January-February) of the vernal phase, with the temporal severity of the outbreak (growth of daily COVID-19 deaths) in Eurasia peaking in the vernal equinoctial period (late March-late April),

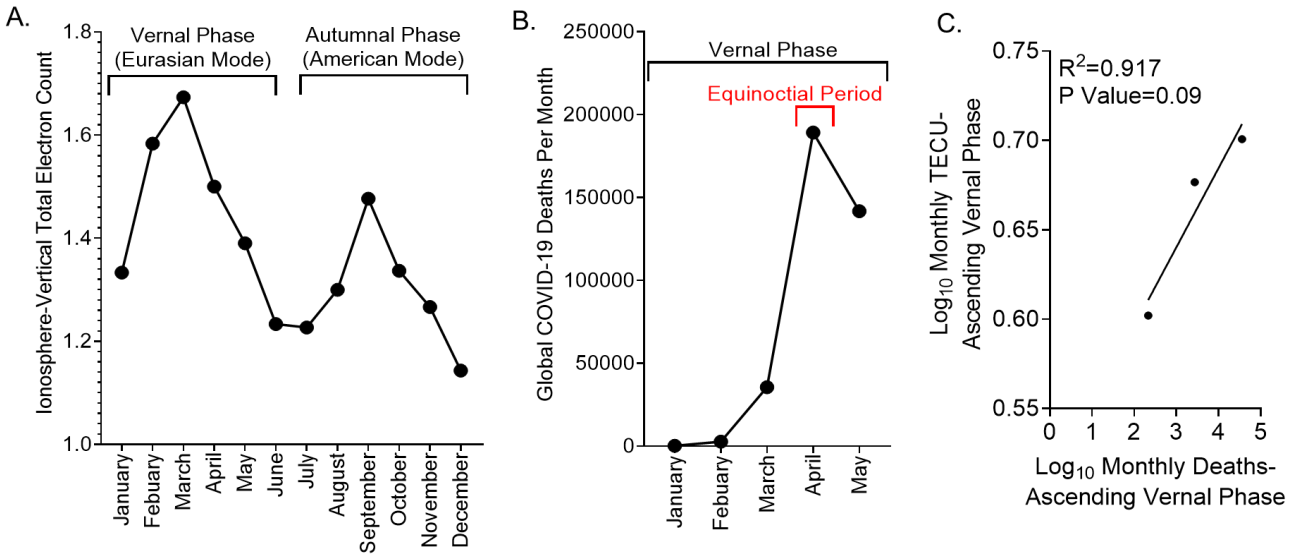

Figure 12: The epidemic curve of severe COVID-19 outbreaks are/will be synchronous with the semi-annual oscillations of the geomagnetic field intensity. (A) The lithospheric component of the geomagnetic field and the associated long-wavelength magnetic anomalies are coupled to the ionospheric magnetic field. Analysis of the temporal dynamics of the geomagnetic magnetic field in the northern hemisphere via ionospheric-vertical total electron count (TECU) measurements from global navigational satellites in 2016 (a solar minimum) by Parwani, M. et al, 2019 (Russian Journal of Earth Sciences, VOL. 19, ES1003, doi:10.2205/2018ES000644, 2019), demonstrates the well-established semi-annual oscillation, with two maxima in the equinoctial period and the two minima in the solstitial period. The total electron count per month value represents the mean for measurements from locations in the United States, China and Norway. The vernal phase is designated as the Eurasian mode and the autumnal phase is designated the American mode, based on previous pattern of the relative oscillations of the weakening geomagnetic field between Eurasia and North America. (B-C) Analysis of the global temporal dynamics of severe COVID-19 outbreaks (global deaths per month) (Our World In Data as of May 21, 2020) demonstrates a synchronous relationship with geomagnetic field oscillations, with severe COVID-19 outbreaks (global deaths per month) peaking in the vernal equinoctial period and subsequently declining (B). Segmented correlation analysis demonstrate that the temporal dynamics of severe COVID-19 outbreaks is directly associated with the ionospheric-total electron count (a proxy for the lithospheric magnetic field) during the ascending-vernal phase (January – March) (C).

and subsequently declining (**Figure 12, 13**). Here, we propose that the emergence of COVID-19 outbreaks resulted from the generation of LWMAs that exhibit resonance with ferromagnetic-like iron stores in humans, thus enabling the magnetic catalysis of iron oxides-silicate-like minerals and the associated SARS-CoV-2 [137]. The temporal dynamics of the severe COVID-19 outbreaks in Eurasia is synchronous with the temporal dynamics of the ionospheric total electron count (a proxy for the coupled lithospheric component of the geomagnetic field [194, 195]) for the vernal phase, with the peak in COVID-19 death-associated illness occurring at the vernal equinox (based on the 3-week-time to death [173])

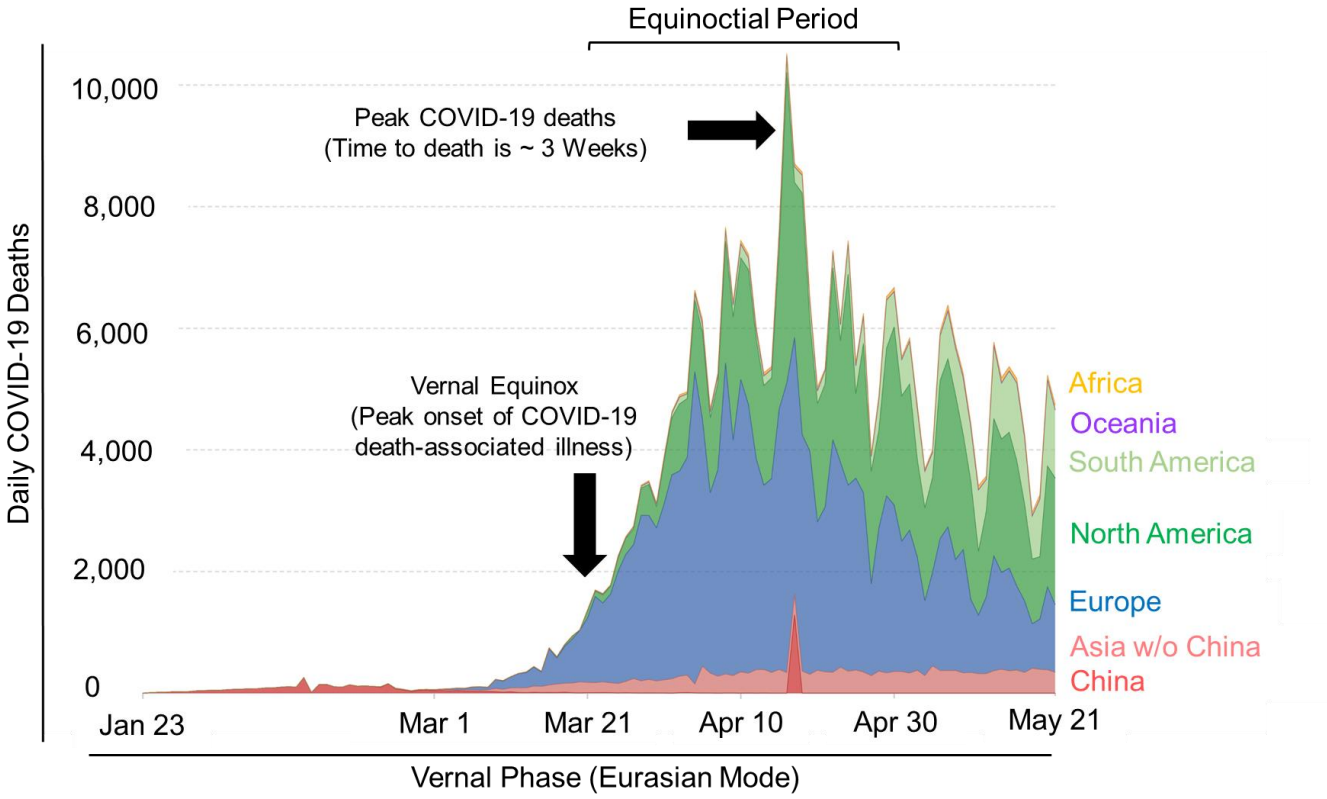

Figure 13: The spatiotemporal dynamics of severe COVID-19 outbreaks are associated with the oscillations of the geomagnetic field intensity and restricted to tectonic plates with Proterozoic cratons. The global temporal dynamics of severe COVID-19 outbreaks in the vernal phase is synchronous with the oscillations of the geomagnetic field intensity and predominately restricted to Eurasia and the Americas. Additionally, the global spatiotemporal dynamics of severe COVID-19 outbreaks mimics a vibrating drumhead, like the vibrating drumhead dynamics of the geomagnetic field intensity. The median time to death for COVID-19 in the vernal phase is ~3 weeks after the onset of illness; thus, there is a ~3 weeks backward shift in the peak at the equinox for the onset of illness associated with the peak daily death.

(**Figure 12, 13**) [196]. Severe COVID-19 outbreaks in North America also peaked in the vernal equinoctial period (late March-late April) (**Figure 12, 13**) [196]. We propose that the temporal severity of COVID-19 outbreaks in Eurasia and North America in the autumnal phase will be synchronous with the autumnal phase of the geomagnetic field intensity oscillation; thus, the second peak of severe COVID-19 outbreaks is predicted in the autumnal equinoctial period (late September-late October) (**Figure 12, 13**) [196]. Based on the predictions by Bility, M. T., 2019 [105], we propose that COVID-19 outbreaks in North America in 2019 were misidentified as the vaping-associated severe acute respiratory syndrome disease, which affected a relatively small number of high-risked individuals (namely, vapors/electronic cigarette users with high levels of iron oxides nanoparticles in their lungs due to the use of Kanthal (iron alloy)-quartz rods heating element) [197-200]. Indeed, a recent study by Shivani Mathur Gaiha et al. demonstrated that vaping significantly increases the risk of COVID-19 in youths in North America [201]. The vaping-associated severe acute respiratory syndrome disease exhibited symptomology, lung, and kidney diseases, with silicate/glass-like pathologies and iron oxide-like deposits (i.e., black particles), similar to COVID-19 [197-200, 202]. Furthermore, the temporal dynamics of the vaping-associated severe acute respiratory syndrome disease outbreak (daily hospitalizations) in North America is similar to the temporal dynamics of COVID-19 outbreaks (daily deaths) in North America, with the epidemic emerging in the vernal equinoctial period, stabilizing during the solstitial period, increasing after the summer solstice, peaking around the autumnal equinox, and subsequently declining [198, 200]. Therefore, we propose that the global epidemic curve of severe COVID-19 outbreaks (daily deaths over time) exhibit a semiannual oscillation, with two maxima in the equinoctial periods (late March-late April; late September-late October), and two minima around the solstices (late June-late July;

late December-late January)[196], along with a quasi-biannual oscillation between years, in consistence with the geomagnetic field (and component lithospheric magnetic field) dynamics (**Figure 12, 13**) [203-205]. Furthermore, in consistence with the hypothesis that COVID-19 outbreaks are governed by geomagnetic field dynamics [206], the global spatiotemporal dynamics of COVID-19 outbreaks mimics a vibrating drumhead-like dynamics. Although the spatiotemporal dynamics and the intensity of the weakening geomagnetic field varies yearly, the previous pattern suggests relative oscillations between Western Eurasia (in the vernal phase) and the Americas (in the autumnal phase) [207]; thus, we retrodict that the vernal

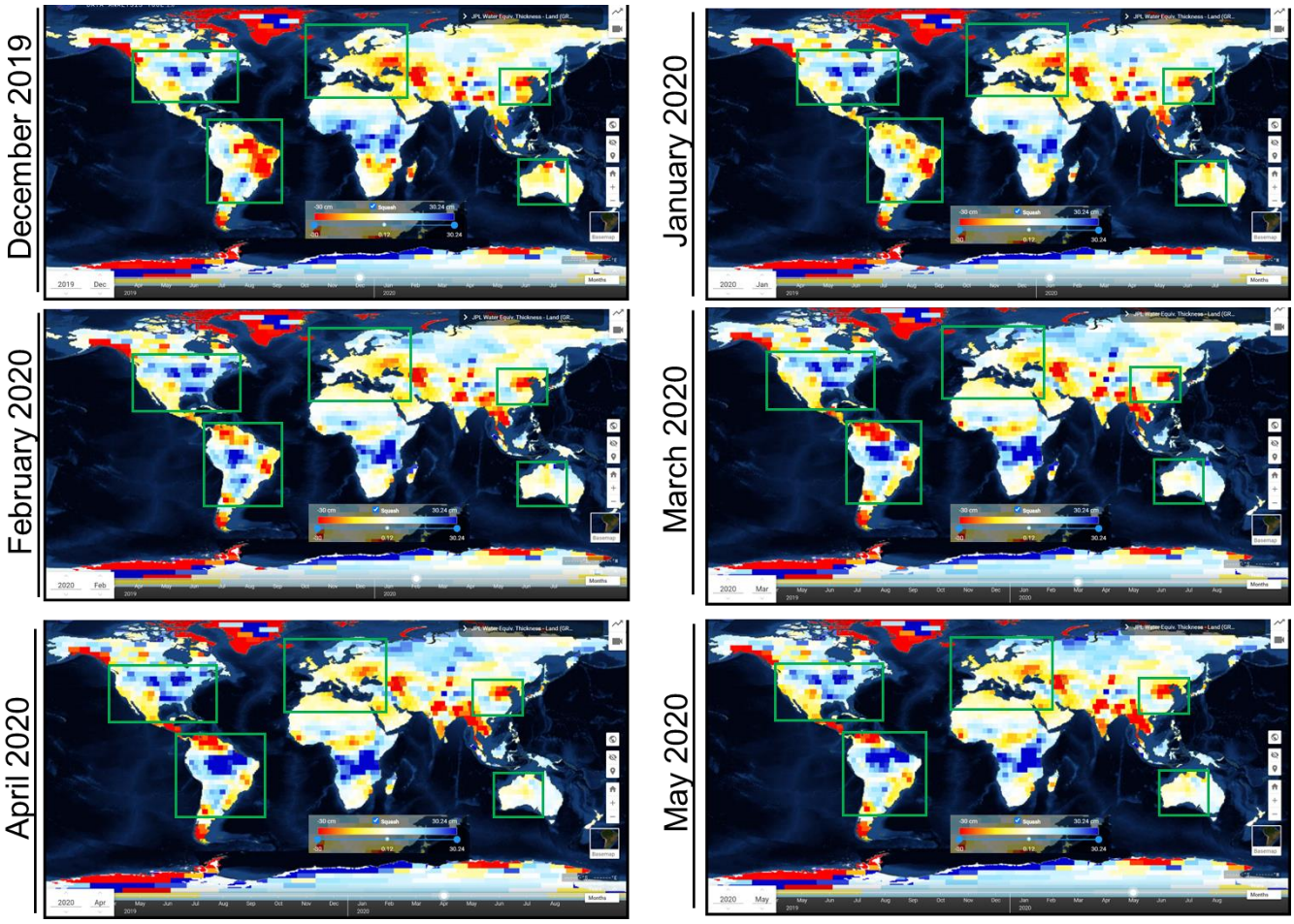

Figure 14: Severe COVID-19 outbreaks are spatiotemporally associated with terrestrial water storage (TWS) dynamics in tectonic plates with Proterozoic cratons. The maps of TWS anomaly in tectonic plates with Proterozoic cratons (green boxes) during the vernal phase of the COVID-19 pandemic demonstrate that regions with more severe COVID-19 outbreaks were wetter, and vice versa. The maps were generated by NASA's Jet Propulsion Laboratory (JPL) using GRACE/GRACE-FO satellite data.

phase of the epidemic coincided with the Western Eurasian mode and predict that the autumnal phase of the epidemic will coincide with the American mode.

3.5 The spatiotemporal relationship between serpentinization-associated water storage and severe COVID-19 outbreaks in tectonic plates with Proterozoic cratons

The spatiotemporal dynamics of terrestrial water storage in the lithosphere modulates the serpentinization of peridotites and the generation of ferromagnetic-like iron oxides-silicate rock minerals and the associated magnetic anomalies [182, 208]. Therefore, terrestrial water storage is a significant determinant of severe COVID-19 outbreaks in tectonic plates with Proterozoic cratons [182]. Here, we propose that precipitation (excess wetness)-associated increased in terrestrial water storage modulates the vernal equinoctial maximum of

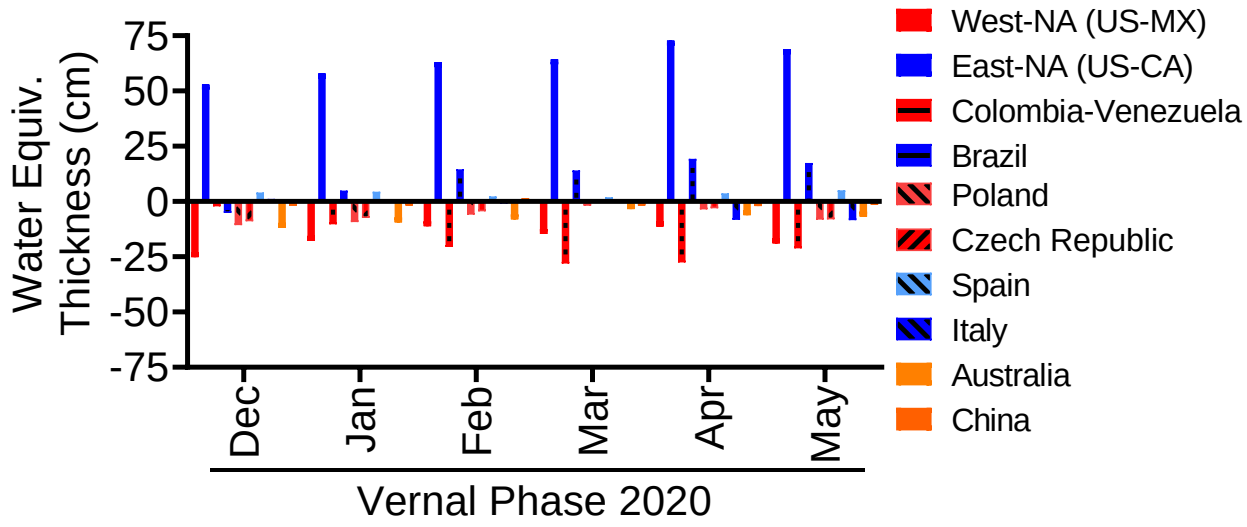

Figure 15: The regional differences in the severity of COVID-19 outbreaks within tectonic plates with Proterozoic cratons is associated with terrestrial water storage (TWS) dynamics. Analysis of TWS anomaly in basins in tectonic plates with Proterozoic cratons during the vernal phase of the COVID-19 pandemic. TWS analysis were performed for major basins in North America (NA), (mostly in the United States (US), West NA, US and Mexico-MX: Colorado, Rio Grande, Columbia, San Joaquin; East NA, US and Canada-CA: Mississippi, Saint Lawrence, Saguenay, Churchill), South America (Brazil-Amazon and Parana; Eastern Colombia and Venezuela-Orinoco), Western Eurasia (Spain-Douro, Italy-Po, Czech Republic-Elbe, Poland-Odra), Eastern Eurasia (China-Yangtze/Chang Jiang), Australia (Mackey), with high or low severity of COVID-19 outbreaks. The reddish and bluish colors denote river basins with low and high TWS anomalies, respectively, and regions with low and high severity of COVID-19 outbreaks, respectively. The values presented denotes the sum or the value of the TWS anomaly of the major basins in the respective region.

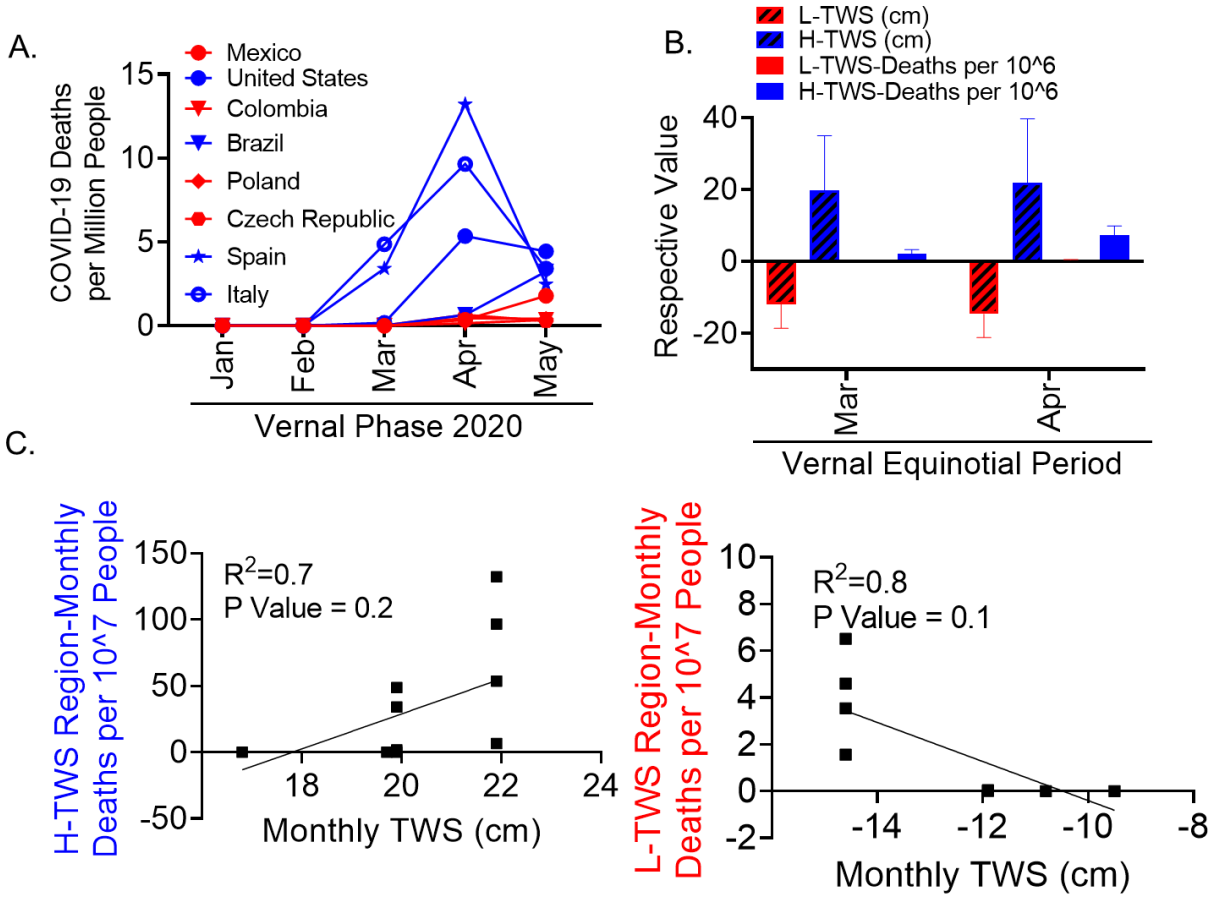

Figure 16: The severity of COVID-19 outbreaks within tectonic plates with Proterozoic cratons in the vernal phase is associated with increase terrestrial water storage. (A) Analysis of severe COVID-19 outbreaks within the Eurasian and American tectonic plates during the vernal phase demonstrates regional differences within the same plate, with regions with high terrestrial water storage (TWS) anomaly exhibiting severe outbreaks (Blue color), while region with low TWS anomaly exhibiting less severe outbreaks (Red color). TWS analysis were performed for basins within the North American (NA) plate (Northeastern NA-United States: Mississippi, Saint Lawrence, Saguenay, Churchill; Southwestern NA-Mexico: Grand de Santiago, Rio Grande), South America (SA) plate (Central SA-Brazil: Amazon and Parana; Northern SA-Eastern Colombia and Venezuela: Orinoco), Western Eurasia (WE, Europe) plate (Western Europe: Spain-Douro, Italy-Po; Eastern Europe: Czech Republic-Elbe, Poland-Odra. (B) Analysis of the severity of COVID-19 outbreaks (by Our World In Data) and TWS anomaly in the Eurasian and American tectonic plates during the vernal equinoctial period demonstrates an association between TWS and the COVID-19 deaths per million people, with high-TWS regions (H-TWS) exhibiting higher deaths per million people than low-TWS regions (L-TWS). The values presented denote the mean and standard deviation of the TWS anomaly or deaths per million in the respective anomaly group. The P values for Analysis of variance (ANOVA) for TWS: Month=0.85, Region=0.1, TWS anomaly group (Low or High)<0.0001; Deaths per million people: Month=0.026, Region=0.055, TWS anomaly group (Low or High)=0.057. (C) Segmented correlation analysis for the asending vernal phase of TWS (January-April) for regions with high-TWS (H-TWS) demonstrates that TWS is directly associated with the severity of COVID-19 outbreaks in wetter regions. On the contrary, regions with low-TWS (LWS) exhibit an inverse relationship between TWS and the COVID-19 deaths per population; albiet drier regions had significantly less severe outbreaks, than wetter regions in the vernal phase.

serpentinization-induced COVID-19-LWMAs, while evaporation (excess dryness)-associated decreased in terrestrial water storage modulates the autumnal equinoctial maximum of serpentinization-induced COVID-19-LWMAs [209-211]; as demonstrated in the serpentinization-driven carbon dioxide mineralization in the Ronda peridotites (Western Eurasia) [182]. Analysis of the terrestrial water storage anomaly in tectonic plates with significant Proterozoic cratons in the vernal phase of the recorded COVID-19 pandemic (December 2019-May 2020) using GRACE Satellite Data Analysis Tool (National Aeronautics and Space Administration, NASA) [212] demonstrates that basins with severe COVID-19 outbreaks are associated with increased terrestrial water storage (wetter regions) and vice visa (**Figure 14, 15, 16**) [182]. We predict that basin regions with severe COVID-19 outbreaks in the autumnal phase will be spatiotemporally associated with decreased terrestrial water storage (excess dryness) and vice visa [182].

3.6 Public health implications of the magnetic catalysis-induced COVID-19 hypothesis

The current public health understanding and response to the SARS-CoV-2-associated COVID-19 pandemic is based on the germ theory [213, 214]. Currently, it is presumed that the COVID-19 pandemic began with a zoonotic transmission of a SARS-CoV-2-like virus from animal(s) to human(s) in the Yangtze River basin (Wuhan, Hubei, China) on the Proterozoic-Yangtze craton in late 2019 and that severe COVID-19 outbreaks are due to person-to-person transmission [215, 216]. Therefore, stay-at-home restrictions, social distancing (>6 feet apart), and the use of facemasks are employed to control the pandemic [215, 216]. Furthermore, the global epidemic curve of SARS-CoV-2-associated COVID-19 outbreaks, with the maximum in the equinoctial period and the minimum in the solstitial period is currently ascribed to those

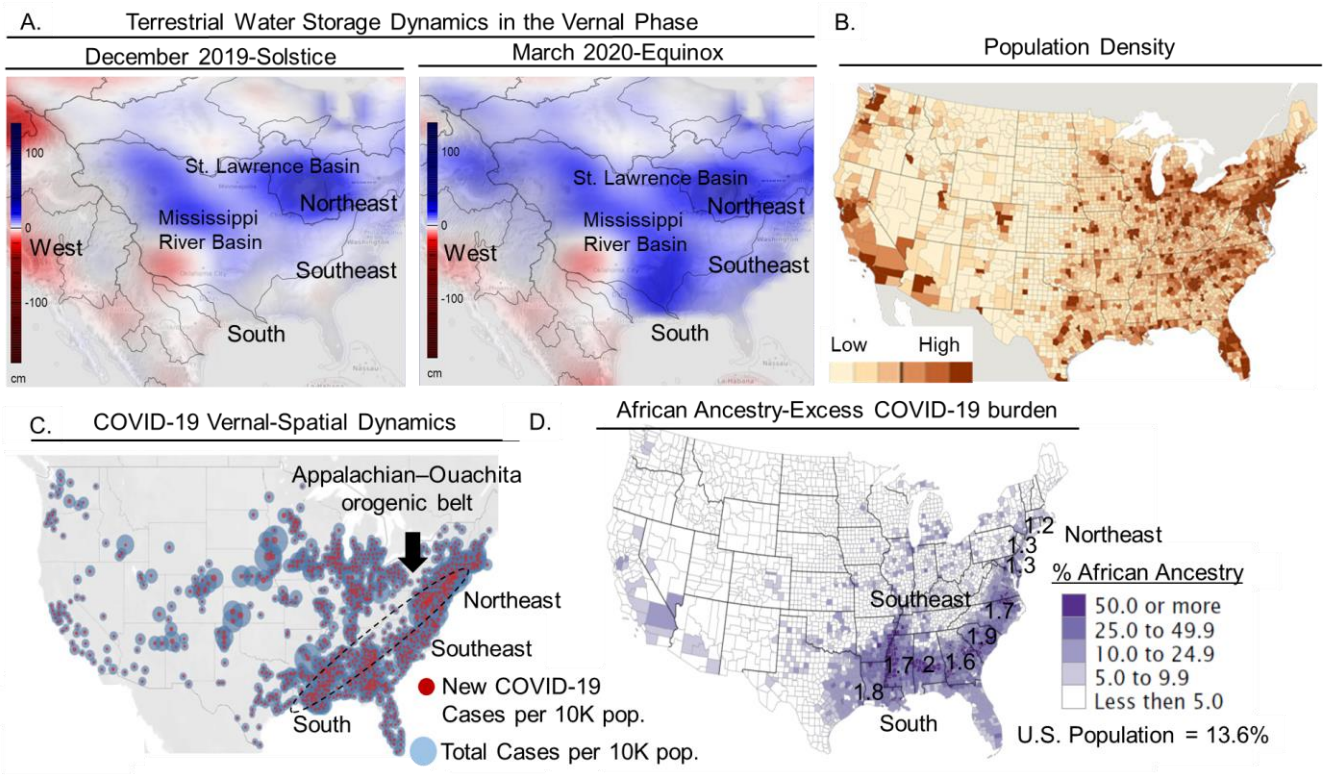

Figure 17: The disproportionate severity of the COVID-19 epidemic in populations with African Ancestry on the North American plate in the vernal phase co-localized with increased terrestrial water storage. (A) The maps of TWS dynamics (GravIS - GFZ German Research Centre for Geosciences) in the North American plate for the solstial and equinoctial periods demonstrates that the eastern portion of the United States (U.S.) became wetter during the equinoctial period, whereas the western portion remained relatively dry. (B-C) The eastern half of the U.S. has a similar population density as the coastal regions in the western portion of the U.S. (per U.S. Census Bureau, 2011), however, those regions exhibited significant differences in the severity of the COVID-19 outbreaks in the vernal phase (Note: cases includes both disease and asymptomatic cases). Census legend: The light color (light tan; low) regions denotes less than 10 people per square mile and the dark color area (bark brown; high) denotes equal to or greater than 300 people per square mile. The increased wetness in the eastern portion of the U.S. during the equinoctial period was associated with more severe COVID-19 outbreaks (and associated deaths, not shown). The river basins in the Appalachian-Ouachita orogenic belt (black-hatch marks) in the eastern half of the U.S. experienced the highest increase in TWS and the most severe COVID-19 outbreaks. The COVID-19 epidemic map legend: The map displays the new (red, latest week) and total (blue) cases per 10,000 people (10K pop.) as of May 25, 2020. The cases size ranges from 5, 500, 1000, to >1500 cases per 10,000 people (the map was generated by John Hopkins University). (D) Populations with African ancestry in the U.S. predominately (~90%) reside in the so-called black belt, which spans the basins in the Appalachian-Ouachita orogenic belt (U.S. Census Bureau, The 2010 Census Briefs, The Black Population: 2010; Issued September 2011). Populations of African ancestry predominately reside in the low-lying, flood prone regions in those coastal basins and have higher exposure to increased TWS levels. Analysis of the COVID-19 pandemic in the vernal phase (April 13, 2020) demonstrate populations with African ancestry have excess death burden compared to populations with non-African ancestry (Note: The values within each state denotes the excess death relative to the state's population. The COVID-19 data obtained from Samantha Artiga et al, April, 21, 2020, Kaiser Family Foundation).

public health interventions. However, the germ theory and associated models have been incapable of making accurate long-term predictions about the spatiotemporal dynamics of COVID-19 outbreaks [214]. Furthermore, those germ theory-derived models cannot explain the differential severity of the COVID-19 pandemic within countries and continental regions or across tectonic plates without using ad-hoc immunizing hypotheses that cannot be falsified [214]. These ad hoc-immunizing hypotheses include the argument that Peru's severe COVID-19 outbreak, despite early and highly restrictive lockdown, is due to the developing nation status of the country and the associated economic weakness (Virus Exposes Weak Links in Peru's Success Story, by Mitra Taj and Anatoly Kurmanaev on June 12, 2020, New York Times). On the contrary, an ad hoc-immunizing hypothesis for the less severe COVID-19 outbreaks in Africa posits that the developing nation status of those countries and the associated limited interaction with the global economy reduced the severity of COVID-19 outbreaks (Think 168,000 Ventilators Is Too Few? Try Three, by Graeme Wood on April 10, 2020, The Atlantic; Coronavirus in South Africa: Scientists explore surprise theory for low death rate, by Andrew Harding, BBC) [79]. South Africa, which lies in the South Atlantic Anomaly and contains a Proterozoic range with

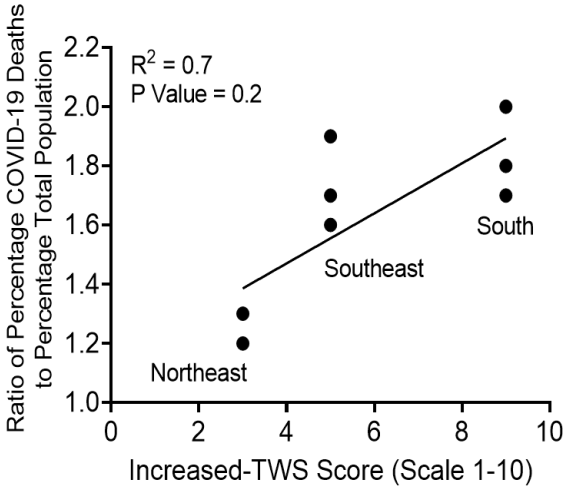

Figure 18: The disproportionate COVID-19-induced death burden in African Ancestry populations on the North American plate in the vernal phase is associated with higher exposure to increased terrestrial water storage. Analysis of increased TWS score (March 2020) in the basin regions in the Greater Appalachian-Ouachita orogenic belt (the so-called black belt) during the vernal phase of the COVID-19 pandemic demonstrate an association between the disproportionate impact of the COVID-19 pandamic (cumulative data on April 13, 2020) on populations with African ancestry and the increased levels of TWS exposure (COVID-19 data obtained from Samantha Artiga et al, published on April, 21, 2020, Kaiser Family Foundation).

active serpentinization-associated production of serpentine and iron oxides (the southern cape conductive belt) [217, 218] is the only country on the African plate with severe COVID-19 outbreaks [79]. Indeed, South Africa, with less than 5% of the population in Africa, accounts for approximately 50% of the COVID-19 deaths in Africa [219]. The severe COVID-19 outbreaks in South Africa compared to the rest of Africa cannot be ascribed to differences in ethnicity (so-called genetic differences), age demographics, health burdens, economic activities, molecular diagnostic capacity, or social-political factors [79]. Botswana, which borders South Africa and lies at the edge of the South Atlantic Anomaly, has not experienced a severe COVID-19 outbreak, despite shared ethnic-cultural groups (predominately, Bantu tribes), similar age demographic (median age 24-27), underling health burdens (i.e., HIV/AIDS, Tuberculosis and obesity) and economic development/activities (i.e., mining and tourism) with South Africa [220-222]. Additionally, the disproportionate severity of COVID-19 outbreaks in South Africa emerged despite the early and stringent governmental interventions to enforce the germ theory-derived public health measures (i.e., social distancing, the wearing of facemasks) [79, 223]. Additionally, the divergent dynamics of COVID-19 outbreaks on the North American plate in the early autumnal phase, with increasing new COVID-19 deaths in the western portion (i.e., California) and decreasing new COVID-19 deaths in the northeastern portion (i.e., New York) has been ascribed to cultural-sociopolitical differences concerning the adherence to the germ theory-derived public health measures (i.e., social distancing, the use of face mask) (Coronavirus: What's behind alarming new US outbreaks? by Holly Honderich and Ritu Prasad on June 30, 2020, BBC News). However, similar arguments are used to describe the reverse of that COVID-19 spatiotemporal dynamic during the vernal equinoctial period (Why New York has 14 times as many coronavirus deaths as California, by German Lopez on April 13, 2020,

Vox). We argue that ascribing the divergent spatiotemporal dynamics of new COVID-19 deaths in Northeastern and Western North America (United States) to cultural-sociopolitical differences is an ad-hoc immunizing hypothesis. The northeastern (i.e., New York City) and western (i.e., Los Angeles) megacities of North America (United States) have similar populations (including a high level of human movement between those regions), social-political environments, and economic development/activities. Indeed, analysis of social distancing and masking adherence in western (i.e., California) and northeastern (New York) North America (United States) demonstrates similar levels (**Supplementary Figure 1, 2, 3**). However, the northeastern (i.e., New York) and western (i.e., California) portions of North America (United States) exhibit divergent dynamics of terrestrial water storage, which we propose results in the divergent temporal dynamics of the severity of the COVID-19 outbreaks [224-226]. Terrestrial water storage dynamics also account for the disproportionate deaths in populations with African ancestry in the United States during the vernal phase of the COVID-19 pandemic. Individuals with African ancestry disproportionally reside in basins within the coastal belt of the Greater Appalachian-Ouachita orogenic belt that spans the South to the Northeastern United States (the so-called Black belt) (**Figure 17, 18**). This so-called Black belt region has been experiencing increased terrestrial water storage over the past decades [224-226] and experienced increased terrestrial water storage during the vernal phase of the COVID-19 pandemic (**Figure 17, 18**). Indeed, a recent report by the National Academies of Sciences, Engineering, and Medicine (*Framing the Challenge of Urban Flooding in the United States, 2019*) stated that individuals with African ancestry disproportionally reside in the low lying-flood prone areas in those coastal basins [227]. This geographic concentration of individuals with African ancestry in low lying-flood prone areas (*de facto* racial segregation) is due in part to the

geographic locations of the historical-slave states, historical racial segregation laws and customs, and the continued economic disparity in the United States [228]. Thus, COVID-19 outbreaks disproportionally affected peoples with African ancestry in the United States during the vernal phase of the COVID-19 pandemic in part due to their geographic concentration in low lying-flood prone areas in the megacities within the coastal belt that spans the South to the Northeastern United States (the so-called Black belt). Indeed the disproportional COVID-19-induced mortality in the African American population is directly associated with increased terrestrial water storage exposure in the vernal phase (**Figure 17, 18**). Air pollution has been proposed within the germ theory paradigm as a co-determinant of COVID-19-induced mortality in the urban regions of North America (United States) and other parts of the world during the vernal phase of the pandemic [229, 230]. Thus, interventions against air pollution have been proposed as a means of directly reducing COVID-19-induced mortality [229, 230]. The assertion that air pollution accounts for the severity of COVID-19 outbreaks is contradicted by global-scale analysis, which shows that the tectonic plates with the highest COVID-19-mortality burden (the North American, South American, and Western Eurasian tectonic plates) have the lowest air population (**Supplementary Figure 4**) [231]. In contrast, continental regions with the lowest COVID-19-mortality burden (the African, Indian, and Eastern Eurasian tectonic plates) have the highest air population (**Supplementary Figure 4**). Urban regions are the industrial regions (regions with air pollution generating-human activities [231]) in most countries [232-239], and they are predominately located in river basins with relatively higher terrestrial water storage [240]. Therefore, regional (i.e., county/province) analysis within a country will demonstrate a direct association between the severity of COVID-19 outbreaks and the air pollution during the vernal phase of the pandemic [232], albeit, that association does not exist

for continental (i.e., tectonic plates) analysis at the global scale (**Supplementary Figure 4**). A temperate climate condition and reduced solar radiation have been proposed as a major determinant of severe COVID-19 outbreaks in North America (United States) and other regions [241-243]; however, severe COVID-19 outbreaks occurred in divergent climate and solar radiation conditions (**Supplementary Figure 5**) [244]. The proposed serpentinization-induced lithospheric LWMAs mediated severe COVID-19 outbreaks hypothesis provides a means to predict the spatiotemporal dynamics of severe COVID-19 outbreaks using empirical data obtained from magnetometry and gravimetry satellites as demonstrated in Bility, M.T., 2019 [105]. Like current responses to natural disasters, the nowcasting and forecasting of COVID-19-LWMAs using those empirical data could enable better mitigation strategies. Additionally, the development of personal protective equipment/devices, such as Nephrite-Jade amulets [34], which may readily interact with and abrogate serpentinization-induced LWMAs, may provide a means of shielding humans and preventing COVID-19. Furthermore, biomedical interventions targeting ferromagnetic-like iron stores (i.e., iron chelators-deferoxamine [172, 174, 175, 245]) in high-risk groups or diseased individuals may provide a means of preventing and ameliorating COVID-19.

3.7 Strengths and limitations of the magnetic catalysis-mediated COVID-19 hypothesis

A limitation of this study is the lack of sequence data for the coronavirus producing the SARS-CoV-2-like nucleocapsid and spike antigens and a comparative genomic analysis with the SARS-CoV-2 virus in humans in Pittsburgh, Pennsylvania, and the northeastern United States. Indeed, outbreaks of a COVID-19-like disease in minks on isolated farms in Western Eurasia (Spain and The Netherlands) demonstrated that emerging SARS-CoV-2-like viruses in animals

and humans within an isolated geographic location exhibit similarity in their sequences, albeit differences exist [246]. Furthermore, that study demonstrates similar hemorrhagic lung disease as observed in our study, thus providing additional evidence that animal colonies are susceptible to outbreaks of lethal COVID-19-like disease and associated SARS-CoV-2-like infection in the absence of experimental induction [246]. A limitation of this study is that we did not examine vaping-associated severe acute respiratory syndrome disease tissues from 2019 for the presence of the SARS-CoV-2 virus. Another limitation of this study is the lack of data identifying the lithospheric magnetic field-spherical harmonics that mediate severe COVID-19 outbreaks. Furthermore, this study did not identify the electromagnetic wave that mediates COVID-19. These limitations will be addressed in future studies. In this study, we proposed a hypothesis for the SARS-CoV-2-associated COVID-19 pandemic based on an approximately 7,000-6,000 years old knowledge system (Hemudu and Majiabang-Traditional Chinese Medicine) that emerged on the Proterozoic-Yangtze craton during severe geological and geophysical conditions that are similar to the current conditions of the Holocene [4, 14]. The scientific frameworks and concepts employed in the proposed hypothesis, namely, 1) the carbonate-silicate geochemical cycle and the associated generation of magnetic anomalies via serpentinization of peridotites in a weakened geomagnetic field [21], 2) chiral-induced spin selectivity effect in biological molecules [58], and 3) magnetic catalysis [122, 123, 247] are well-established. This work provides a hypothesis (including the mechanism of disease) along with supporting evidence for the role of serpentinization-induced resonant LWMAs in mediating the spatiotemporal dynamics of SARS-CoV-2-associated COVID-19 outbreaks. Most important, the proposed hypothesis meets the criteria of a robust scientific hypothesis [248-251]; namely, 1) it is grounded in well-established scientific frameworks and concepts, 2)

provides a unifying and self-consistent framework that accounts for the empirical evidence, including the so-called anomalies and paradoxes within the current dominant paradigm (the germ theory), 3) makes falsifiable predictions (as demonstrated in Bility, M.T., 2019 [105]) and retrodictions, which can be readily examined by others using empirical evidence, and 4) it does not employ logical fallacies that appeal to emotion (i.e., sociopolitical-cultural affiliation) or authority (i.e., status within society). Additionally, this hypothesis addressed the well-established limitations of the germ theory in describing and predicting the phenomenology of the SARS-CoV-2-associated COVID-19 pandemic.

4. Conclusion

In conclusion, for the first time, we provide a hypothesis, which posits that the carbonate-silicate geochemical cycle and associated geological-geophysical changes mediate human disease, namely, SARS-CoV-2-associated COVID-19. Using insights from Neolithic-Traditional Chinese Medicine (and other Indigenous Knowledge), and the chiral-induced spin selectivity effect in biomolecules, we provide evidence supporting a hypothesis, which posits serpentinization-induced lithospheric LWMAs in Proterozoic cratons, in a weakened geomagnetic field, mediate SARS-CoV-2-associated COVID-19 outbreaks via the magnetic catalysis of iron oxides-silicate-like minerals and SARS-CoV-2 from biogenic molecules in humans. Humans and component biogenic molecules are a form a condensed matter [252, 253]; thus significant limitations exists in the germ theory as it ignores well-established concepts (i.e., chiral-induced spin selectivity) in condensed matter physics. This work seeks to advance the science of public health, as it lays the foundation for the unification of dynamics in

the ferromagnetic-like iron-containing human-biosphere and geosphere via the empirical laws and the theoretical frameworks of condensed matter physics [252, 254].

CRediT author statement

Moses Turkle Bility: Conceptualization, Methodology, Data curation, Visualization, Investigation, Supervision, Writing-Original draft preparation, Reviewing and Editing; Sara Ho: Data curation, Writing-Reviewing, and Editing; Yash Agarwal: Data curation, Writing-Reviewing, and Editing; Isabella Castronova: Data curation, Writing-Reviewing, and Editing; Cole Beatty: Data curation, Writing-Reviewing, and Editing; Shivkumar Biradar: Data curation, Writing-Reviewing, and Editing; Vanshika Narala: Data curation, Writing-Reviewing, and Editing; Nivitha Periyapatna: Data curation, Writing-Reviewing, and Editing; Yue Chen: Investigation; Jean Nachega: Investigation, Writing-Reviewing, and Editing.

Declaration of competing interest

The authors declare no conflict of interest.

Acknowledgments

Grant and funding source: This work was funded through grants from the United States-National Institute of Health (R21AI135412, R21OD024789).

Other contributions: The graphical abstract was contructed via modifying a publically available image created by U.S. Government, The National Oceanic and Atmospheric Administration. We also thank the creators/authors of the maps, datasets, databases used in this publication.

Supplementary Figures

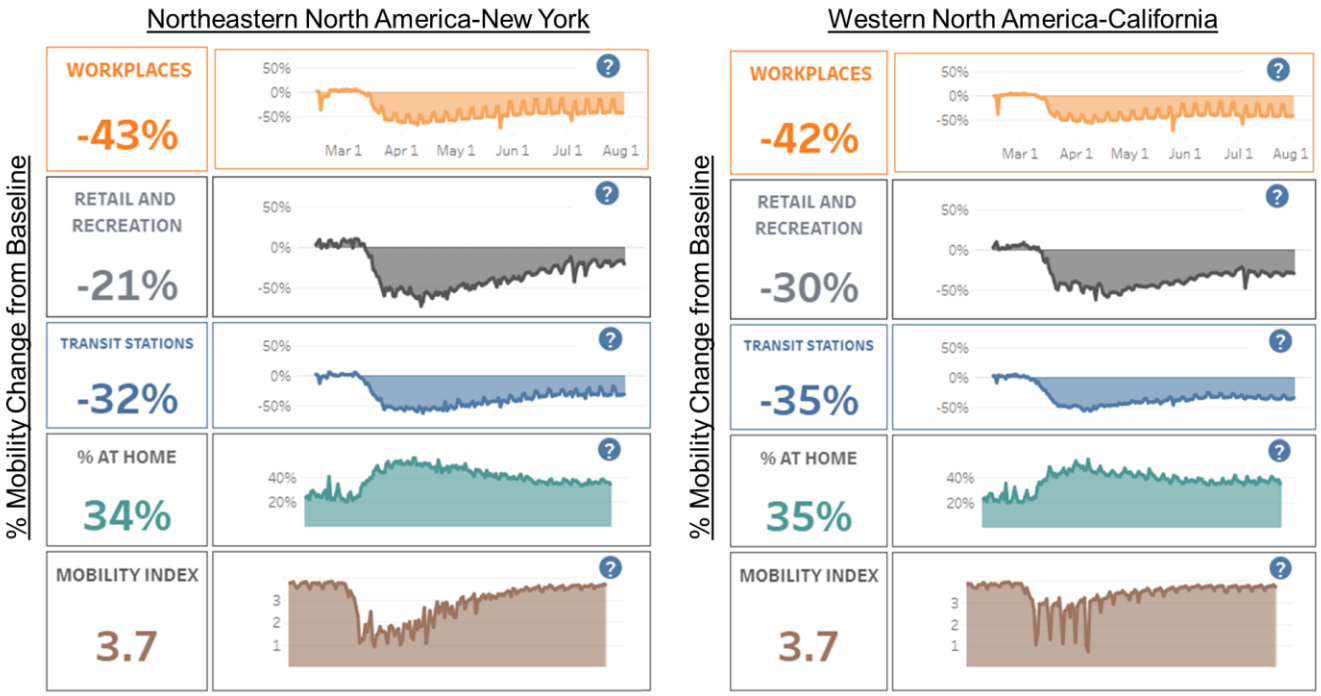

Supplementary Figure 1: Social distancing levels are similar in the western and northeastern United States during the COVID-19 pandemic. Representative analysis of social distancing (transit use, workplace congregation, retail-recreational activities) in the northeastern (left) and western (right) United States demonstrate similar levels. The data was derived by the Center for Disease Control, United States during the COVID-19 pandemic (https://www.cdc.gov/covid-data-tracker/#mobility).

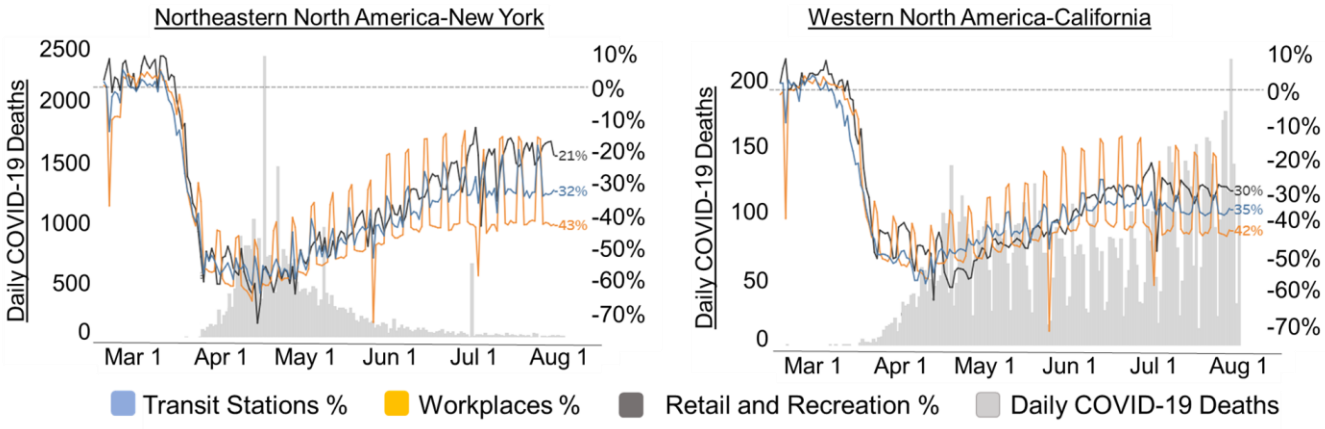

Supplementary Figure 2: Social distancing is not a determinant of the differences in the severity of COVID-19 outbreaks between the western and northeastern United States. Representative analysis of social distancing (transit use, workplace congregation, retail-recreational activities) in the northeastern (left) and western (right) portions of the United States as derived by the Center for Disease Control, United States demonstrate similar levels overtime, despite significant differences in the severity of the COVID-19 outbreaks in those regions (https://www.cdc.gov/covid-data-tracker/#mobility). Although the increasing new COVID-19 deaths in the western portion of the United States after the summer solstice is associated with reduced social distancing, similar reduction in social distancing in the northeastern portion of the United States is associated with decreasing new COVID-19 deaths. This divergent regional outcome associated with reduced social distancing during the ongoing COVID-19 pandemic suggests that social distancing is not a determinant of severe COVID-19 outbreaks.

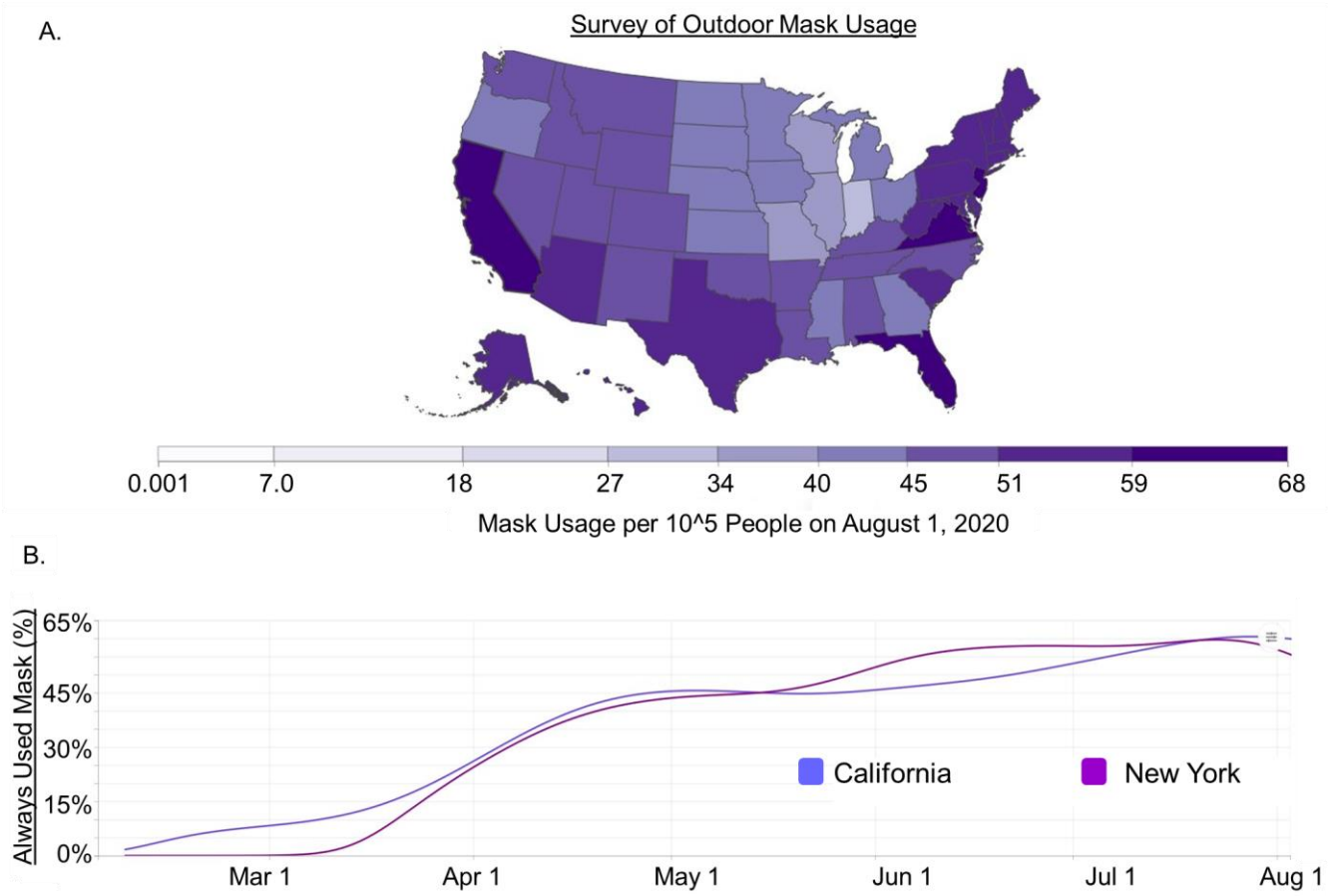

Supplementary Figure 3: Facemask usage is not a determinant of the differences in the severity of COVID-19 outbreaks between the western and northeastern United States. (A-B) Responses to a survey demonstrates similar facemask useage (wears mask at all times outside) in western and northeastern United States (August 1, 2020). Furthermore, analysis of facemask usage between western (i.e., California) and northeastern (i.e., New York) United States overtime, also demonstrate similar levels of usage. The anlysis was performed by Healthdata.org. The data sources: The research data is based on survey results from University of Maryland Social Data Science Center, Kaiser Family Foundation; YouGov COVID-19 Behaviour Tracker survey (http://covid19.healthdata.org/united-states-of-america/california?view=mask-use&tab=map).

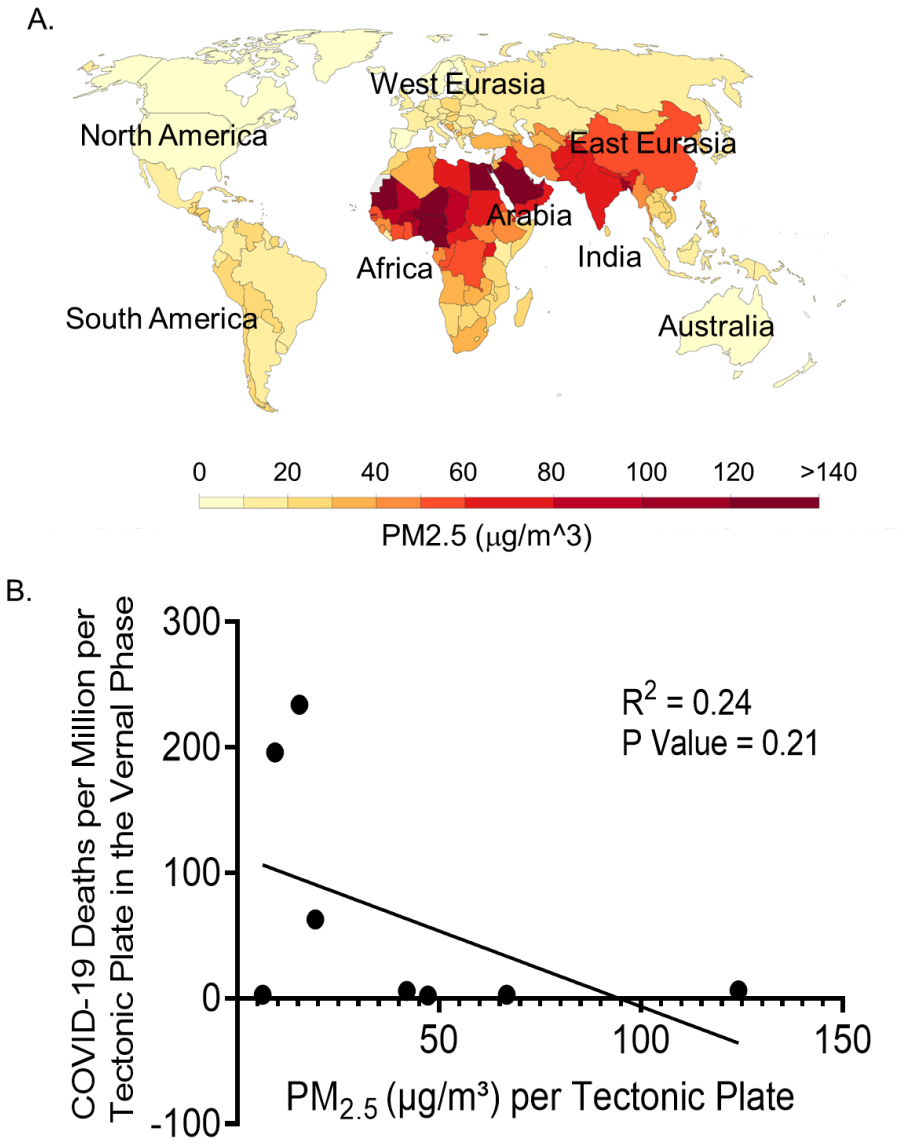

Supplementary Figure 4: Air pollution does not account for the severe COVID-19 outbreaks in Western Eurasia (Europe) and Americas. (A) The population-weighted average level of exposure to concentrations of suspended particles measuring less than 2.5 microns in diameter for the countries on the tectonic plates. Exposure levels is measured in micrograms per cubic metre (μg/m³). The American plates and the Western portion of the Eurasian plate have the highest COVID-19 burden, and the lowest air pollution levels. Whereas, regions on the Africa plate, Indian plate and the East Eurasian plate, have the highest air population levels and the lowest COVID-19 burden. (B) Analysis of the relationship between air pollution on the tectonic plates and severe COVID-19 outbreaks in the vernal phase demonstrate an inverse relationship. The air pollution data was obtained from The World Bank for 1990-2016 and analyzed by the Our World In Data (https://ourworldindata.org/ grapher/pm25-air-pollution). The data source is Brauer, M. et al. 2016, for the Global Burden of Disease Study 2016. The COVID-19 data was obtained from the John Hopkins University-Coronavirus Center, ending on May 21, 2020

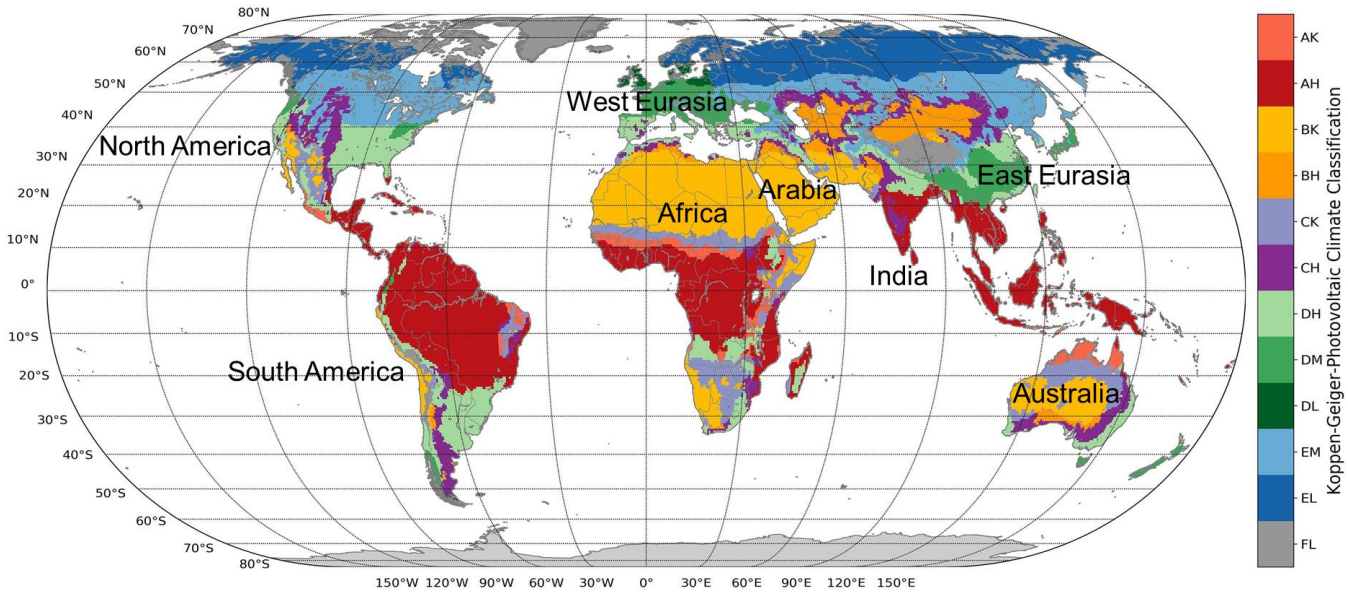

Supplementary Figure 5: Climate is not a determinant of severe COVID-19 outbreaks. The world map of the Koppen-Geiger-Photovoltaic climate classification system as developed by Julián Ascencio-Vásquez et al, 2019 (Solar Energy, Volume 191, October 2019, Pages 672-685) demonstrate regions in the North and South American plates and the Western portion of the Eurasian plate that have the highest COVID-19 burden have varied climate conditions, which exist in other parts of the world with lower COVID-19 burden. Köppen-Geiger-Photovoltaic climate classification with the 12 most relevant climate zones is delineated below. The first letter indicates the Temperature-Precipitation (*TP*)-zones: A-Tropical, B-Desert, C-Steppe, D-Temperate, E-Cold and F- Polar. The second letter indicates the Irradiation (*I*)-zones: K-Very High, H-High, M-Medium and L-Low irradiation.

References

1. Channell, J.E.T. and L. Vigliotti, *The Role of Geomagnetic Field Intensity in Late Quaternary Evolution of Humans and Large Mammals.* Reviews of Geophysics, 2019. **57**(3): p. 709-738.
2. Shennan, S., et al., *Regional population collapse followed initial agriculture booms in mid-Holocene Europe.* Nature Communications, 2013. **4**.
3. Batt, C.M., et al., *Advances in archaeomagnetic dating in Britain: New data, new approaches and a new calibration curve.* Journal of Archaeological Science, 2017. **85**: p. 66-82.
4. Nilsson, A., et al., *Reconstructing Holocene geomagnetic field variation: new methods, models and implications.* Geophysical Journal International, 2014. **198**(1): p. 229-248.
5. Riris, P. and M. Arroyo-Kalin, *Widespread population decline in South America correlates with mid-Holocene climate change.* Sci Rep, 2019. **9**(1): p. 6850.
6. Warden, L., et al., *Climate induced human demographic and cultural change in northern Europe during the mid-Holocene.* Sci Rep, 2017. **7**(1): p. 15251.
7. Li, Y., N. Wang, and C. Zhang, *An abrupt centennial-scale drought event and mid-holocene climate change patterns in monsoon marginal zones of East Asia.* PLoS One, 2014. **9**(3): p. e90241.
8. Walczak, M.H., et al., *A 17,000 yr paleomagnetic secular variation record from the southeast Alaskan margin: Regional and global correlations.* Earth and Planetary Science Letters, 2017. **473**: p. 177-189.
9. Finlay, C.C., J. Aubert, and N. Gillet, *Gyre-driven decay of the Earth's magnetic dipole.* Nature Communications, 2016. **7**: p. 8.
10. Foley, B.J. and P.E. Driscoll, *Whole planet coupling between climate, mantle, and core: Implications for rocky planet evolution.* Geochemistry Geophysics Geosystems, 2016. **17**(5): p. 1885-1914.
11. Olson, P., *Mantle control of the geodynamo: Consequences of top-down regulation.* Geochemistry Geophysics Geosystems, 2016. **17**(5): p. 1935-1956.
12. Van Der Meer, D.G., et al., *Plate tectonic controls on atmospheric CO2 levels since the Triassic.* Proc Natl Acad Sci U S A, 2014. **111**(12): p. 4380-5.
13. Indermuhle, A., et al., *Holocene carbon-cycle dynamics based on CO2 trapped in ice at Taylor Dome, Antarctica.* Nature, 1999. **398**(6723): p. 121-126.
14. Eric, J.S., *Mid-Holocene Climate Change.* Science (American Association for the Advancement of Science), 1999. **286**(5444): p. 1485-1487.
15. Marcott, S.A., et al., *A reconstruction of regional and global temperature for the past 11,300 years.* Science, 2013. **339**(6124): p. 1198-201.
16. Park, H.S., et al., *The impact of Arctic sea ice loss on mid-Holocene climate.* Nat Commun, 2018. **9**(1): p. 4571.
17. Golledge, N.R., et al., *Global environmental consequences of twenty-first-century ice-sheet melt.* Nature, 2019. **566**(7742): p. 65-72.
18. Reager, J.T., et al., *A decade of sea level rise slowed by climate-driven hydrology.* Science, 2016. **351**(6274): p. 699-703.
19. Miriyala, P., et al., *Increased chemical weathering during the deglacial to mid-Holocene summer monsoon intensification.* Sci Rep, 2017. **7**: p. 44310.

20. Gislason, S.R., et al., *Direct evidence of the feedback between climate and weathering.* Earth and Planetary Science Letters, 2009. **277**(1-2): p. 213-222.
21. Ortiz, E., et al., *Geophysical Characterization of Serpentinite Hosted Hydrogeology at the McLaughlin Natural Reserve, Coast Range Ophiolite.* Geochemistry Geophysics Geosystems, 2018. **19**(1): p. 114-131.
22. Beinlich, A., et al., *Peridotite weathering is the missing ingredient of Earth's continental crust composition.* Nature Communications, 2018. **9**.
23. Lamadrid, H.M., et al., *Effect of water activity on rates of serpentinization of olivine.* Nat Commun, 2017. **8**: p. 16107.
24. Nemani, R., et al., *Recent trends in hydrologic balance have enhanced the terrestrial carbon sink in the United States.* Geophysical Research Letters, 2002. **29**(10): p. 4.
25. Thébault, E., et al., *The Magnetic Field of the Earth's Lithosphere.* Space science reviews, 2010. **155**(1-4): p. 95-127.
26. Dashtdar, M., et al., *The Concept of Wind in Traditional Chinese Medicine.* Journal of Pharmacopuncture, 2016. **19**(4): p. 293-302.
27. Hewlett, B.S. and R.P. Amola, *Cultural contexts of Ebola in northern Uganda.* Emerging Infectious Diseases, 2003. **9**(10): p. 1242-1248.
28. Hewlett, B.S. and R.P. Amola, *Cultural contexts of Ebola in northern Uganda.* Emerg Infect Dis, 2003. **9**(10): p. 1242-8.
29. Darvill, T., *Roads to Stonehenge: A prehistoric healing centre and pilgrimage site in southern Britain.* In A Ranft & Schenkluhn, W (eds), Kulturstraßen als Konzept, 2016. **20 Jahre Straße der Romani**(Regensburg: Schell & Steiner.): p. 155–166.
30. Franks, L.J., *Stone medicine : a Chinese medical guide to healing with gems and minerals*. 2016, Rochester, Vermont: Healing Arts Press. xxiv, 488 pages, 32 unnumbered pages of plates.
31. Dematte, P., *The Chinese Jade age - Between antiquarianism and archaeology.* Journal of Social Archaeology, 2006. **6**(2): p. 202-226.
32. Wilson, M.S., *Chinese Jade from the Neolithic to the Qing - Rawson,J.* Apollo-the International Magazine of the Arts, 1996. **143**(409): p. 61-62.
33. He, K.Y., et al., *Middle-Holocene sea-level fluctuations interrupted the developing Hemudu culture in the lower Yangtze River, China.* Quaternary Science Reviews, 2018. **188**: p. 90-103.
34. Harlow, G.E. and S.S. Sorensen, *Jade (Nephrite and Jadeitite) and Serpentinite: Metasomatic connections.* International Geology Review, 2005. **47**(2): p. 113-146.
35. Huang, T.M., *Liangzhu - a Late Neolithic Jade-Yielding Culture in Southeastern Coastal China.* Antiquity, 1992. **66**(250): p. 75-83.
36. Gibaja-Bao, J.F., *Jade: Sign objects and social interpretation of Alpine jades in neolithic Europe.* European Journal of Archaeology, 2018. **21**(3): p. 483-487.
37. Terradas, X., *JADE. Objects-signs and social interpretations of Alpine jade in Neolithic Europe.* Trabajos De Prehistoria, 2017. **74**(2): p. 383-385.
38. Odriozola, C.P., J.A.G. Cordero, and R.V. Garcia, *JADE: Social interpretations of object-signs of Alpine jades in Neolithic Europe.* Antiquity, 2017. **91**(360): p. 1668-1671.
39. Gauthier, E. and P. Petrequin, *Social Interpretations of the Transfers of Alpine Jades Axe-heads in the Neolithic Europe Spatial Analysis in the Framework of the ANR Program JADE 2.* Archeosciences-Revue D Archeometrie, 2017. **41**(1): p. 7-23.

40. Odriozola, C.P., *Jade. Large alpine azeheads in Neolithic europe. V and IV millenium B.C.* European Journal of Archaeology, 2015. **18**(1): p. 158-161.
41. D'Amico, C., et al., *Eclogites, jades and other HP-metaophiolites employed for prehistoric polished stone implements in Italy and Europe.* Periodico Di Mineralogia, 2004. **73**: p. 17-42.
42. Damico, C., et al., *Eclogites and Jades as Prehistoric Implements in Europe - a Case of Petrology Applied to Cultural-Heritage.* European Journal of Mineralogy, 1995. **7**(1): p. 29-41.
43. Kostov, R.I., et al., *Micro-PIXE Geochemical Fingerprinting of Nephrite Neolithic Artifacts from Southwest Bulgaria.* Geoarchaeology, 2012. **27**(5): p. 457-469.
44. Mizumoto, K., K. Kagaya, and G. Chowell, *Early epidemiological assessment of the transmission potential and virulence of coronavirus disease 2019 (COVID-19) in Wuhan City, China, January-February, 2020.* BMC Med, 2020. **18**(1): p. 217.
45. Tang, Y.-J., et al., *Widespread refertilization of cratonic and circum-cratonic lithospheric mantle.* Earth-science reviews, 2013. **118**: p. 45-68.
46. Hong, H., et al., *Clinical characteristics of novel coronavirus disease 2019 (COVID-19) in newborns, infants and children.* Pediatr Neonatol, 2020. **61**(2): p. 131-132.
47. Yang, W., et al., *Clinical characteristics and imaging manifestations of the 2019 novel coronavirus disease (COVID-19):A multi-center study in Wenzhou city, Zhejiang, China.* J Infect, 2020.
48. Siordia, J.A., Jr., *Epidemiology and clinical features of COVID-19: A review of current literature.* J Clin Virol, 2020. **127**: p. 104357.
49. Karmin, M., et al., *A recent bottleneck of Y chromosome diversity coincides with a global change in culture.* Genome Research, 2015. **25**(4): p. 459-466.
50. Tian, S., et al., *Pulmonary pathology of early phase 2019 novel coronavirus (COVID-19) pneumonia in two patients with lung cancer.* J Thorac Oncol, 2020.
51. Su, H., et al., *Renal histopathological analysis of 26 postmortem findings of patients with COVID-19 in China.* Kidney Int, 2020.
52. Guan, W.J., et al., *Clinical Characteristics of Coronavirus Disease 2019 in China.* N Engl J Med, 2020.
53. Lei, J., et al., *CT Imaging of the 2019 Novel Coronavirus (2019-nCoV) Pneumonia.* Radiology, 2020: p. 200236.
54. Tian, S., et al., *Pathological study of the 2019 novel coronavirus disease (COVID-19) through postmortem core biopsies.* Mod Pathol, 2020.
55. Fox, S.E., et al., *Pulmonary and cardiac pathology in African American patients with COVID-19: an autopsy series from New Orleans.* Lancet Respir Med, 2020.
56. Ghosh, S., et al., *Effect of Chiral Molecules on the Electron's Spin Wavefunction at Interfaces.* Journal of Physical Chemistry Letters, 2020. **11**(4): p. 1550-1557.
57. Naaman, R., Y. Paltiel, and D.H. Waldeck, *Chiral molecules and the electron spin.* Nature Reviews Chemistry, 2019. **3**(4): p. 250-260.
58. Naaman, R., *Chiral molecules and the electron's spin: A new pathway to spin selective chemistry.* Abstracts of Papers of the American Chemical Society, 2019. **257**.
59. Naaman, R., D.H. Waldeck, and Y. Paltiel, *Chiral molecules-ferromagnetic interfaces, an approach towards spin controlled interactions.* Applied Physics Letters, 2019. **115**(13).

60. Buchachenko, A.L. and V.L. Berdinsky, *Spin catalysis as a new type of catalysis in chemistry.* Uspekhi Khimii, 2004. **73**(11): p. 1123-1130.
61. Buchachenko, A.L. and V.L. Berdinsky, *Spin catalysis as a nuclear spin selective process.* Chemical Physics Letters, 1998. **298**(4-6): p. 279-284.
62. Buchachenko, A.L. and V.L. Berdinsky, *Spin catalysis of chemical reactions.* Journal of Physical Chemistry, 1996. **100**(47): p. 18292-18299.
63. Minaev, B.F. and H. Agren, *Spin-Orbit-Coupling Induced Chemical-Reactivity and Spin-Catalysis Phenomena.* Collection of Czechoslovak Chemical Communications, 1995. **60**(3): p. 339-371.
64. Buchachenko, A.L. and V.L. Berdinsky, *Electron spin catalysis.* Chemical Reviews, 2002. **102**(3): p. 603-612.
65. Lassmann, G., et al., *Electron-Spin-Resonance Investigation of Tyrosyl Radicals of Prostaglandin-H Synthase - Relation to Enzyme Catalysis.* Journal of Biological Chemistry, 1991. **266**(30): p. 20045-20055.
66. Khavryuchenko, V.D., O.V. Khavryuchenko, and V.V. Lisnyak, *Effect of spin catalysis in H2S oxidation: A quantum chemical insight.* Catalysis Communications, 2010. **11**(5): p. 340-345.
67. Buchachenko, A.L., *Mass-independent isotope effects.* J Phys Chem B, 2013. **117**(8): p. 2231-8.
68. Filev, V. and R. Rashkov, *Magnetic Catalysis of Chiral Symmetry Breaking: A Holographic Prospective.* Advances in High Energy Physics, 2010. **2010**: p. 56.
69. Khavryuchenko, O.V., V.D. Khavryuchenko, and D.S. Su, *Spin catalysts: A quantum trigger for chemical reactions.* Chinese Journal of Catalysis, 2015. **36**(10): p. 1656-1661.
70. Gusynin, V.P., V.A. Miransky, and I.A. Shovkovy, *Catalysis of Dynamical Flavor Symmetry Breaking by a Magnetic Field in 2+1 Dimensions.* Phys Rev Lett, 1994. **73**(26): p. 3499-3502.
71. Casanova, J.L. and L. Abel, *The genetic theory of infectious diseases: a brief history and selected illustrations.* Annu Rev Genomics Hum Genet, 2013. **14**: p. 215-43.
72. Paul, M., *Seasonality in infectious diseases: does it exist for all pathogens?* Clin Microbiol Infect, 2012. **18**(10): p. 925-6.
73. Fisman, D.N., *Seasonality of infectious diseases.* Annu Rev Public Health, 2007. **28**: p. 127-43.
74. Altizer, S., et al., *Seasonality and the dynamics of infectious diseases.* Ecol Lett, 2006. **9**(4): p. 467-84.
75. Dowell, S.F. and M.S. Ho, *Seasonality of infectious diseases and severe acute respiratory syndrome-what we don't know can hurt us.* Lancet Infect Dis, 2004. **4**(11): p. 704-8.
76. Hirve, S., et al., *Influenza Seasonality in the Tropics and Subtropics - When to Vaccinate?* PLoS One, 2016. **11**(4): p. e0153003.
77. Chinazzi, M., et al., *The effect of travel restrictions on the spread of the 2019 novel coronavirus (COVID-19) outbreak.* Science, 2020. **368**(6489): p. 395-400.
78. Gilbert, M., et al., *Preparedness and vulnerability of African countries against importations of COVID-19: a modelling study.* Lancet, 2020. **395**(10227): p. 871-877.
79. Mbow, M., et al., *COVID-19 in Africa: Dampening the storm?* Science, 2020. **369**(6504): p. 624-626.

80. Iwasaki, A. and N.D. Grubaugh, *Why does Japan have so few cases of COVID-19?* EMBO Molecular Medicine, 2020. **12**(5): p. e12481-n/a.
81. Iwasaki, A. and N.D. Grubaugh, *Why does Japan have so few cases of COVID-19?* EMBO molecular medicine, 2020. **12**(5): p. e12481.
82. Accinelli, R.A. and J.A. Leon-Abarca, *At High Altitude COVID-19 Is Less Frequent: The Experience of Peru.* Arch Bronconeumol, 2020.
83. Quevedo-Ramirez, A., et al., *Altitude and excess mortality during COVID-19 pandemic in Peru.* Respir Physiol Neurobiol, 2020. **281**: p. 103512.
84. Del Brutto, O.H., et al., *SARS-CoV-2-related mortality in a rural Latin American population.* Int J Infect Dis, 2020.
85. Daughton, A.R., R. Chunara, and M.J. Paul, *Comparison of Social Media, Syndromic Surveillance, and Microbiologic Acute Respiratory Infection Data: Observational Study.* JMIR Public Health Surveill, 2020. **6**(2): p. e14986.
86. Aghaali, M., et al., *Performance of Bayesian outbreak detection algorithm in the syndromic surveillance of influenza-like illness in small region.* Transbound Emerg Dis, 2020.
87. Salamatbakhsh, M., K. Mobaraki, and J. Ahmadzadeh, *Syndromic Surveillance System for MERS-CoV as New Early Warning and Identification Approach.* Risk Manag Healthc Policy, 2020. **13**: p. 93-95.
88. Smith, S., et al., *Investigating regional variation of respiratory infections in a general practice syndromic surveillance system.* J Public Health (Oxf), 2020.
89. Sokhna, C., et al., *Senegal's Grand Magal of Touba: Syndromic Surveillance during the 2016 Mass Gathering.* Am J Trop Med Hyg, 2020. **102**(2): p. 476-482.
90. Xie, J.G. and Y.J. Zhu, *Association between ambient temperature and COVID-19 infection in 122 cities from China.* Science of the Total Environment, 2020. **724**.
91. Ascencio-Vasquez, J., K. Brecl, and M. Topic, *Methodology of Koppen-Geiger-Photovoltaic climate classification and implications to worldwide mapping of PV system performance.* Solar Energy, 2019. **191**: p. 672-685.
92. Price-Haywood, E.G., et al., *Hospitalization and Mortality among Black Patients and White Patients with Covid-19.* N Engl J Med, 2020. **382**(26): p. 2534-2543.
93. Fouad, M.N., J. Ruffin, and S.M. Vickers, *COVID-19 Is Disproportionately High in African Americans. This Will Come as No Surprise.* Am J Med, 2020.
94. Raisi-Estabragh, Z., et al., *Greater risk of severe COVID-19 in Black, Asian and Minority Ethnic populations is not explained by cardiometabolic, socioeconomic or behavioural factors, or by 25(OH)-vitamin D status: study of 1326 cases from the UK Biobank.* J Public Health (Oxf), 2020.
95. Feschotte, C. and C. Gilbert, *Endogenous viruses: insights into viral evolution and impact on host biology.* Nat Rev Genet, 2012. **13**(4): p. 283-96.
96. Theze, J., et al., *Remarkable diversity of endogenous viruses in a crustacean genome.* Genome Biol Evol, 2014. **6**(8): p. 2129-40.
97. Katzourakis, A. and R.J. Gifford, *Endogenous viral elements in animal genomes.* PLoS Genet, 2010. **6**(11): p. e1001191.
98. Wu, X.D., et al., *Serological tests facilitate identification of asymptomatic SARS-CoV-2 infection in Wuhan, China.* Journal of Medical Virology, 2020.
99. Long, Q.X., et al., *Clinical and immunological assessment of asymptomatic SARS-CoV-2 infections.* Nature Medicine, 2020.

100. Merad, M. and J.C. Martin, *Pathological inflammation in patients with COVID-19: a key role for monocytes and macrophages.* Nat Rev Immunol, 2020. **20**(6): p. 355-362.
101. Park, M.D., *Macrophages: a Trojan horse in COVID-19?* Nat Rev Immunol, 2020. **20**(6): p. 351.
102. Anderson, J.M., A. Rodriguez, and D.T. Chang, *Foreign body reaction to biomaterials.* Semin Immunol, 2008. **20**(2): p. 86-100.
103. Heald-Sargent, T., et al., *Age-Related Differences in Nasopharyngeal Severe Acute Respiratory Syndrome Coronavirus 2 (SARS-CoV-2) Levels in Patients With Mild to Moderate Coronavirus Disease 2019 (COVID-19).* JAMA Pediatr, 2020.
104. Lee, S., et al., *Clinical Course and Molecular Viral Shedding Among Asymptomatic and Symptomatic Patients With SARS-CoV-2 Infection in a Community Treatment Center in the Republic of Korea.* JAMA internal medicine, 2020.
105. Bility, M.M.T., *Are rises in the Lithosphere-Magnetic Field in the United States, interacting with vaping aerosols-iron in lungs, the tipping point for the outbreak of vaping-associated acute lung injury?* ResearchGate 2019(November).
106. Edson, A.R., et al., *The carbonate-silicate cycle and CO2/climate feedbacks on tidally locked terrestrial planets.* Astrobiology, 2012. **12**(6): p. 562-71.
107. Caldeira, K., *Continental-pelagic carbonate partitioning and the global carbonate-silicate cycle.* Geology, 1991. **19**: p. 204-6.
108. Brady, P.V., *THE EFFECT OF SILICATE WEATHERING ON GLOBAL TEMPERATURE AND ATMOSPHERIC CO2.* Journal of Geophysical Research-Solid Earth, 1991. **96**(B11): p. 18101-18106.
109. Idoko, C.M., et al., *The potential contribution to long wavelength magnetic anomalies from the lithospheric mantle.* Physics of the Earth and Planetary Interiors, 2019. **292**: p. 21-28.
110. Aubert, J., C.C. Finlay, and A. Fournier, *Bottom-up control of geomagnetic secular variation by the Earth's inner core.* Nature, 2013. **502**(7470): p. 219-23.
111. Finlay, C.C., J. Aubert, and N. Gillet, *Gyre-driven decay of the Earth's magnetic dipole.* Nature Communications, 2016. **7**.
112. Huang, R.F., et al., *The production of iron oxide during peridotite serpentinization: Influence of pyroxene.* Geoscience Frontiers, 2017. **8**(6): p. 1311-1321.
113. Mishra, D.C., *Long Wavelength Magnetic-Anomalies from the Lithosphere - Indian Shield and Himalaya.* Tectonophysics, 1984. **105**(1-4): p. 319-330.
114. Tang, Y.J., et al., *Widespread refertilization of cratonic and circum-cratonic lithospheric mantle.* Earth-Science Reviews, 2013. **118**: p. 45-68.
115. Lougheed, M.S. and J.J. Mancuso, *Biogenic Origin of Lake-Superior Precambrian Iron-Formations.* Economic Geology, 1975. **70**(7): p. 1324-1324.
116. Laberge, G.L., *Possible Biological Origin of Precambrian Iron-Formations.* Economic Geology, 1973. **68**(7): p. 1098-1109.
117. Canfield, D.E., et al., *A Mesoproterozoic iron formation.* Proceedings of the National Academy of Sciences of the United States of America, 2018. **115**(17): p. E3895-E3904.
118. Horie, M., et al., *Endogenous non-retroviral RNA virus elements in mammalian genomes.* Nature, 2010. **463**(7277): p. 84-7.
119. Russo, A.G., et al., *Novel insights into endogenous RNA viral elements in Ixodes scapularis and other arbovirus vector genomes.* Virus Evolution, 2019. **5**(1).

120. Meyer, T.J., et al., *Endogenous Retroviruses: With Us and against Us.* Frontiers in Chemistry, 2017. **5**.
121. Miransky, V.A. and I.A. Shovkovy, *Magnetic catalysis and anisotropic confinement in QCD.* Physical Review D, 2002. **66**(4).
122. Gusynin, V.P., V.A. Miransky, and I.A. Shovkovy, *Theory of the magnetic catalysis of chiral symmetry breaking in QED.* Nuclear Physics B, 1999. **563**(1-2): p. 361-389.
123. Semenoff, G.W., I.A. Shovkovy, and L.C.R. Wijewardhana, *Universality and the magnetic catalysis of chiral symmetry breaking.* Physical Review D, 1999. **60**(10).
124. Gusynin, V.P., V.A. Miransky, and I.A. Shovkovy, *Dimensional reduction and catalysis of dynamical symmetry breaking by a magnetic field.* Nuclear Physics B, 1996. **462**(2-3): p. 249-290.
125. Gusynin, V.P., V.A. Miransky, and I.A. Shovkovy, *Catalysis of dynamical flavor symmetry breaking by a magnetic field in 2+1 dimensions (vol 73, pg 3499, 1994).* Physical Review Letters, 1996. **76**(6): p. 1005-1005.
126. Behnia, S., S. Fathizadeh, and A. Akhshani, *DNA Spintronics: Charge and Spin Dynamics in DNA Wires.* Journal of Physical Chemistry C, 2016. **120**(5): p. 2973-2983.
127. Behnia, S. and S. Fathizadeh, *Spintronics in nano scales: An approach from DNA spin polarization.* Scientia Iranica, 2017. **24**(6): p. 3448-3451.
128. Di Ventra, M. and Y.V. Pershin, *SPIN PHYSICS DNA spintronics sees the light.* Nature Nanotechnology, 2011. **6**(4): p. 198-199.
129. Zwolak, M. and M. Di Ventra, *DNA spintronics.* Applied Physics Letters, 2002. **81**(5): p. 925-927.
130. Gohler, B., et al., *Spin Selectivity in Electron Transmission Through Self-Assembled Monolayers of Double-Stranded DNA.* Science, 2011. **331**(6019): p. 894-897.
131. Naaman, R., *Electrons spin and chirality: From molecular spintronics to enantio-recognition.* Abstracts of Papers of the American Chemical Society, 2018. **255**.
132. Naaman, R., *Chirality induced spin selectivity (CISS) effect-chiral molecules for spintronics.* Abstracts of Papers of the American Chemical Society, 2015. **249**.
133. Naaman, R. and D.H. Waldeck, *Spintronics and Chirality: Spin Selectivity in Electron Transport Through Chiral Molecules.* Annual Review of Physical Chemistry, Vol 66, 2015. **66**: p. 263-281.
134. Xie, Z.T., et al., *Spin Specific Electron Conduction through DNA Oligomers (vol 11, pg 4652, 2011).* Nano Letters, 2012. **12**(1): p. 523-523.
135. Buchachenko, A.L., et al., *Magnetic isotope and magnetic field effects on the DNA synthesis.* Nucleic Acids Res, 2013. **41**(17): p. 8300-7.
136. Liu, M.K., et al., *Spontaneous chiral symmetry breaking in metamaterials.* Nature Communications, 2014. **5**: p. 9.
137. Naaman, R., D.H. Waldeck, and Y. Paltiel, *Chiral molecules-ferromagnetic interfaces, an approach towards spin controlled interactions.* Applied Physics Letters, 2019. **115**(13): p. 4.
138. Preiner, M., et al., *Serpentinization: Connecting Geochemistry, Ancient Metabolism and Industrial Hydrogenation.* Life (Basel), 2018. **8**(4).
139. Wichmann, D., et al., *Autopsy Findings and Venous Thromboembolism in Patients With COVID-19.* Ann Intern Med, 2020.
140. Wichmann, D., et al., *Autopsy Findings and Venous Thromboembolism in Patients With COVID-19: A Prospective Cohort Study.* Ann Intern Med, 2020.

141. Rushby, A.J., et al., *Long-Term Planetary Habitability and the Carbonate-Silicate Cycle.* Astrobiology, 2018. **18**(5): p. 469-480.
142. Fredin, O., et al., *The inheritance of a Mesozoic landscape in western Scandinavia.* Nat Commun, 2017. **8**: p. 14879.
143. Colling, M.E. and Y. Kanthi, *COVID-19-associated coagulopathy: An exploration of mechanisms.* Vasc Med, 2020: p. 1358863X20932640.
144. Connors, J.M. and J.H. Levy, *COVID-19 and its implications for thrombosis and anticoagulation.* Blood, 2020. **135**(23): p. 2033-2040.
145. Su, H., et al., *Renal histopathological analysis of 26 postmortem findings of patients with COVID-19 in China.* Kidney Int, 2020. **98**(1): p. 219-227.
146. Schaefer, I.M., et al., *In situ detection of SARS-CoV-2 in lungs and airways of patients with COVID-19.* Mod Pathol, 2020.
147. Carsana, L., et al., *Pulmonary post-mortem findings in a series of COVID-19 cases from northern Italy: a two-centre descriptive study.* Lancet Infect Dis, 2020.
148. Rocha, A.B., et al., *Detection of SARS-CoV-2 in formalin-fixed paraffin-embedded tissue sections using commercially available reagents.* Laboratory Investigation, 2020.
149. Greenberger, R.N., et al., *Serpentinization, iron oxidation, and aqueous conditions in an ophiolite: Implications for hydrogen production and habitability on Mars.* Earth and planetary science letters, 2015. **416**: p. 21-34.
150. Linder, M.C., *Mobilization of stored iron in mammals: a review.* Nutrients, 2013. **5**(10): p. 4022-50.
151. Xu, J.Z., et al., *Impaired Iron Status in Aging Research.* International Journal of Molecular Sciences, 2012. **13**(2): p. 2368-2386.
152. Picca, A., et al., *Advanced Age Is Associated with Iron Dyshomeostasis and Mitochondrial DNA Damage in Human Skeletal Muscle.* Cells, 2019. **8**(12).
153. Ashraf, A., M. Clark, and P.W. So, *The Aging of Iron Man.* Frontiers in Aging Neuroscience, 2018. **10**.
154. Fleming, D.J., et al., *Dietary factors associated with the risk of high iron stores in the elderly Framingham Heart Study cohort.* American Journal of Clinical Nutrition, 2002. **76**(6): p. 1375-1384.
155. Fleming, D.J., et al., *Iron status of the free-living, elderly Framingham Heart Study cohort: an iron-replete population with a high prevalence of elevated iron stores.* American Journal of Clinical Nutrition, 2001. **73**(3): p. 638-646.
156. Ma, A.G., et al., *Iron Storage in Women is Positively Correlated with Aging and BMI Values.* Faseb Journal, 2016. **30**.
157. Grasselli, G., et al., *Baseline Characteristics and Outcomes of 1591 Patients Infected With SARS-CoV-2 Admitted to ICUs of the Lombardy Region, Italy.* JAMA, 2020.
158. Team, C.C.-R., *Coronavirus Disease 2019 in Children - United States, February 12-April 2, 2020.* MMWR Morb Mortal Wkly Rep, 2020. **69**(14): p. 422-426.
159. Zheng, F., et al., *Clinical Characteristics of Children with Coronavirus Disease 2019 in Hubei, China.* Curr Med Sci, 2020.
160. Kim, J.W., et al., *Serum Ferritin Levels Are Positively Associated With Metabolically Obese Normal Weight: A Nationwide Population-Based Study.* Medicine (Baltimore), 2015. **94**(52): p. e2335.
161. Lecube, A., et al., *Factors accounting for high ferritin levels in obesity.* Int J Obes (Lond), 2008. **32**(11): p. 1665-9.

162. Moreno-Navarrete, J.M., et al., *Hepatic iron content is independently associated with serum hepcidin levels in subjects with obesity.* Clin Nutr, 2017. **36**(5): p. 1434-1439.
163. Batchuluun, B., et al., *Serum ferritin level is higher in poorly controlled patients with Type2 diabetes and people without diabetes, aged over 55years.* Diabetic Medicine, 2014. **31**(4): p. 419-424.
164. Simcox, J.A. and D.A. McClain, *Iron and Diabetes Risk.* Cell Metabolism, 2013. **17**(3): p. 329-341.
165. Ma, H., et al., *Serum ferritin levels are associated with insulin resistance in Chinese men and post-menopausal women: the Shanghai Changfeng study.* Br J Nutr, 2018. **120**(8): p. 863-871.
166. Milman, N. and M. Kirchhoff, *Relationship between serum ferritin and risk factors for ischaemic heart disease in 2235 Danes aged 30-60 years.* Journal of Internal Medicine, 1999. **245**(5): p. 423-433.
167. Cheng, W.L., et al., *Determination of serum and erythrocyte iron, serum ferritin, MCH and MCHC related with aged hypertension and coronary heart disease.* Spectroscopy and Spectral Analysis, 1999. **19**(3): p. 383-384.
168. Lee, D.H., et al., *Association between serum ferritin and hypertension according to the working type in Korean men: the fifth Korean National Health and nutrition examination survey 2010-2012.* Ann Occup Environ Med, 2018. **30**: p. 40.
169. Gordeuk, V.R., et al., *Serum ferritin concentrations and body iron stores in a multicenter, multiethnic primary-care population.* Am J Hematol, 2008. **83**(8): p. 618-26.
170. Camaschella, C. and E. Poggiali, *Towards explaining "unexplained hyperferritinemia".* Haematologica, 2009. **94**(3): p. 307-9.
171. Chen, N., et al., *Epidemiological and clinical characteristics of 99 cases of 2019 novel coronavirus pneumonia in Wuhan, China: a descriptive study.* Lancet, 2020. **395**(10223): p. 507-513.
172. Gomez-Pastora, J., et al., *Hyperferritinemia in critically ill COVID-19 patients - Is ferritin the product of inflammation or a pathogenic mediator?* Clin Chim Acta, 2020. **509**: p. 249-251.
173. Zhou, F., et al., *Clinical course and risk factors for mortality of adult inpatients with COVID-19 in Wuhan, China: a retrospective cohort study.* Lancet, 2020. **395**(10229): p. 1054-1062.
174. Ruscitti, P., et al., *Severe COVID-19, Another Piece in the Puzzle of the Hyperferritinemic Syndrome. An Immunomodulatory Perspective to Alleviate the Storm.* Frontiers in immunology, 2020. **11**.
175. Edeas, M., J. Saleh, and C. Peyssonnaux, *Iron: Innocent bystander or vicious culprit in COVID-19 pathogenesis?* Int J Infect Dis, 2020. **97**: p. 303-305.
176. El-Borie, M.A., et al., *The Dependence of Solar, Plasma, and Geomagnetic Parameters' Oscillations on the Heliospheric Magnetic Field Polarities: Wavelet Analysis.* Astrophysical Journal, 2019. **880**(2).
177. Fear, R.C., et al., *How Much Flux Does a Flux Transfer Event Transfer?* Journal of Geophysical Research-Space Physics, 2017. **122**(12): p. 12310-12327.
178. Sabaka, T.J., et al., *CM6: a comprehensive geomagnetic field model derived from both CHAMP and Swarm satellite observations.* Earth Planets and Space, 2020. **72**(1).
179. Sebera, J., et al., *On the Observability of the Time-Variable Lithospheric Signal in Satellite Magnetic Data.* Surveys in geophysics, 2019. **40**(5): p. 1229-1243.

180. Peng, S.B., et al., *Geology, geochemistry, and geochronology of the Miaowan ophiolite, Yangtze craton: Implications for South China's amalgamation history with the Rodinian supercontinent.* Gondwana Research, 2012. **21**(2-3): p. 577-594.
181. Guillot, S., et al., *Tectonic significance of serpentinites.* Tectonophysics, 2015. **646**: p. 1-19.
182. Giampouras, M., et al., *Geochemistry and mineralogy of serpentinization-driven hyperalkaline springs in the Ronda peridotites.* Lithos, 2019. **350**.
183. Zhao, L., et al., *Evidence for a serpentinized plate interface favouring continental subduction.* Nat Commun, 2020. **11**(1): p. 2171.
184. Hirth, G. and S. Guillot, *Rheology and Tectonic Significance of Serpentinite.* Elements, 2013. **9**(2): p. 107-113.
185. Reynard, B., *Serpentine in active subduction zones.* Lithos, 2013. **178**: p. 171-185.
186. Debret, B., et al., *Three steps of serpentinization in an eclogitized oceanic serpentinization front (Lanzo Massif - Western Alps).* Journal of Metamorphic Geology, 2013. **31**(2): p. 165-186.
187. Zumla, A. and M.S. Niederman, *Editorial: The explosive epidemic outbreak of novel coronavirus disease 2019 (COVID-19) and the persistent threat of respiratory tract infectious diseases to global health security.* Curr Opin Pulm Med, 2020. **26**(3): p. 193-196.
188. Baykiev, E., D. Yixiati, and J. Ebbing, *Global High-Resolution Magnetic Field Inversion Using Spherical Harmonic Representation of Tesseroids as Individual Sources.* Geosciences, 2020. **10**(4).
189. Husch, J.M., *PALISADES SILL - ORIGIN OF THE OLIVINE ZONE BY SEPARATE MAGMATIC INJECTION RATHER THAN GRAVITY SETTLING.* Geology, 1990. **18**(8): p. 699-702.
190. Menke, W., et al., *Crustal Heating and Lithospheric Alteration and Erosion Associated With Asthenospheric Upwelling Beneath Southern New England (USA).* Journal of Geophysical Research-Solid Earth, 2018. **123**(10): p. 8995-9008.
191. Zakharova, N.V., et al., *New insights into lithology and hydrogeology of the northern Newark Rift Basin.* Geochemistry Geophysics Geosystems, 2016. **17**(6): p. 2070-2094.
192. Stefanelli, P., et al., *Whole genome and phylogenetic analysis of two SARS-CoV-2 strains isolated in Italy in January and February 2020: additional clues on multiple introductions and further circulation in Europe.* Euro Surveill, 2020. **25**(13).
193. Brufsky, A., *Distinct Viral Clades of SARS-CoV-2: Implications for Modeling of Viral Spread.* J Med Virol, 2020.
194. Thebault, E., et al., *The Magnetic Field of the Earth's Lithosphere.* Space Science Reviews, 2010. **155**(1-4): p. 95-127.
195. Prokhorov, B.E., et al., *Simulated vertical electric field data: An estimation from an improved coupling model for the lithosphere-atmosphere-ionosphere system.* Data Brief, 2019. **26**: p. 104513.
196. Parwani, M., et al., *Latitudinal variation of ionospheric TEC at Northern Hemispheric region.* Russian Journal of Earth Sciences, 2019. **19**(1).
197. Butt, Y.M., et al., *Pathology of Vaping-Associated Lung Injury.* N Engl J Med, 2019. **381**(18): p. 1780-1781.
198. Hswen, Y. and J.S. Brownstein, *Real-Time Digital Surveillance of Vaping-Induced Pulmonary Disease.* N Engl J Med, 2019. **381**(18): p. 1778-1780.

199. Viswam, D., et al., *Respiratory failure caused by lipoid pneumonia from vaping e-cigarettes.* BMJ Case Rep, 2018. **2018**.
200. Hartnett, K.P., et al., *Syndromic Surveillance for E-Cigarette, or Vaping, Product Use-Associated Lung Injury.* N Engl J Med, 2020. **382**(8): p. 766-772.
201. Gaiha, S.M., J. Cheng, and B. Halpern-Felsher, *Association Between Youth Smoking, Electronic Cigarette Use, and Coronavirus Disease 2019.* Journal of adolescent health, 2020.
202. Fels Elliott, D.R., et al., *Giant cell interstitial pneumonia secondary to cobalt exposure from e-cigarette use.* Eur Respir J, 2019. **54**(6).
203. Lyatsky, W. and A.M. Hamza, *Seasonal and diurnal variations of geomagnetic activity and their role in Space Weather forecast.* Canadian Journal of Physics, 2001. **79**(6): p. 907-920.
204. Sebera, J., et al., *On the Observability of the Time-Variable Lithospheric Signal in Satellite Magnetic Data.* Surveys in Geophysics, 2019. **40**(5): p. 1229-1243.
205. Ou, J.M., A.M. Du, and C.C. Finlay, *Quasi-biennial oscillations in the geomagnetic field: Their global characteristics and origin.* Journal of Geophysical Research-Space Physics, 2017. **122**(5): p. 5043-5058.
206. Archer, M.O., et al., *Direct observations of a surface eigenmode of the dayside magnetopause.* Nat Commun, 2019. **10**(1): p. 615.
207. Sheshpari, M., *Seismo-Magnetic Precursors Seen From Space in Magnetosphere Anomaly for Prediction of Earthquakes.* Electronic Journal of Geotechnical Engineering 2017. **22**((12)): p. 4551-4557.
208. Beinlich, A., et al., *Peridotite weathering is the missing ingredient of Earth's continental crust composition.* Nature communications, 2018. **9**(1): p. 634-12.
209. Yi, H. and L.X. Wen, *Satellite gravity measurement monitoring terrestrial water storage change and drought in the continental United States.* Scientific Reports, 2016. **6**.
210. Strassberg, G., B.R. Scanlon, and M. Rodell, *Comparison of seasonal terrestrial water storage variations from GRACE with groundwater-level measurements from the High Plains Aquifer (USA).* Geophysical Research Letters, 2007. **34**(14).
211. Hay, W.W., *Detrital sediment fluxes from continents to oceans.* Chemical Geology, 1998. **145**(3-4): p. 287-323.
212. Tapley, B.D., et al., *Contributions of GRACE to understanding climate change.* Nature Climate Change, 2019. **9**(5): p. 358-369.
213. El-Sadr, W.M. and J. Justman, *Africa in the Path of Covid-19.* N Engl J Med, 2020.
214. Holmdahl, I. and C. Buckee, *Wrong but Useful - What Covid-19 Epidemiologic Models Can and Cannot Tell Us.* N Engl J Med, 2020.
215. Ozma, M.A., et al., *Clinical manifestation, diagnosis, prevention and control of SARS-CoV-2 (COVID-19) during the outbreak period.* Infez Med, 2020. **28**(2): p. 153-165.
216. Li, C., et al., *SARS-CoV-2 and Europe: timing of containment measures for outbreak control.* Infection, 2020. **48**(3): p. 483-486.
217. Weckmann, U., et al., *Magnetotelluric measurements across the Beattie magnetic anomaly and the Southern Cape Conductive Belt, South Africa.* Journal of Geophysical Research-Solid Earth, 2007. **112**(B5).
218. Debeer, J.H., J.S.V. Vanzijl, and D.I. Gough, *The Southern Cape Conductive Belt (South-Africa) - Its Composition, Origin and Tectonic Significance.* Tectonophysics, 1982. **83**(3-4): p. 205-225.

219. Drain, P.K. and N. Garrett, *SARS-CoV-2 pandemic expanding in sub-Saharan Africa: Considerations for COVID-19 in people living with HIV.* EClinicalMedicine, 2020. **22**: p. 100342.
220. Lurie, M.N. and B.G. Williams, *Migration and Health in Southern Africa: 100 years and still circulating.* Health Psychol Behav Med, 2014. **2**(1): p. 34-40.
221. Thami, P.K. and E.R. Chimusa, *Population Structure and Implications on the Genetic Architecture of HIV-1 Phenotypes Within Southern Africa.* Front Genet, 2019. **10**: p. 905.
222. Langen, T.T., *Gender power imbalance on women's capacity to negotiate self-protection against HIV/AIDS in Botswana and South Africa.* Afr Health Sci, 2005. **5**(3): p. 188-97.
223. Mehtar, S., et al., *Limiting the spread of COVID-19 in Africa: one size mitigation strategies do not fit all countries.* Lancet Glob Health, 2020. **8**(7): p. e881-e883.
224. Zou, Z.H., et al., *Divergent trends of open-surface water body area in the contiguous United States from 1984 to 2016.* Proceedings of the National Academy of Sciences of the United States of America, 2018. **115**(15): p. 3810-3815.
225. Cao, Q., et al., *Trends and Interannual Variability in Terrestrial Water Storage Over the Eastern United States, 2003-2016.* Water Resources Research, 2019. **55**(3): p. 1928-1950.
226. Adusumilli, S., et al., *A Decade of Water Storage Changes Across the Contiguous United States From GPS and satellite gravity.* Geophysical Research Letters, 2019. **46**(22): p. 13006-13015.
227. in *Framing the Challenge of Urban Flooding in the United States*. 2019: Washington (DC).
228. Leibbrand, C., et al., *The Great Migration and Residential Segregation in American Cities during the Twentieth Century.* Soc Sci Hist, 2020. **44**(1): p. 19-55.
229. Wu, X., et al., *Exposure to air pollution and COVID-19 mortality in the United States: A nationwide cross-sectional study.* medRxiv, 2020.
230. Heederik, D.J.J., L.A.M. Smit, and R.C.H. Vermeulen, *Go slow to go fast: a plea for sustained scientific rigour in air pollution research during the COVID-19 pandemic.* The European respiratory journal, 2020. **56**(1): p. 2001361.
231. Cohen, A.J., et al., *Estimates and 25-year trends of the global burden of disease attributable to ambient air pollution: an analysis of data from the Global Burden of Diseases Study 2015.* Lancet, 2017. **389**(10082): p. 1907-1918.
232. Liang, D., et al., *Urban Air Pollution May Enhance COVID-19 Case-Fatality and Mortality Rates in the United States.* medRxiv, 2020.
233. Li, L., et al., *Urban-rural disparity in the relationship between ambient air pollution and preterm birth.* Int J Health Geogr, 2020. **19**(1): p. 23.
234. Krecl, P., et al., *Drop in urban air pollution from COVID-19 pandemic: Policy implications for the megacity of Sao Paulo.* Environ Pollut, 2020. **265**(Pt B): p. 114883.
235. Toledo de Almeida Albuquerque, T., J.M. Santos, and M.F. Andrade, *Urban air quality, climate, and pollution: from measurement to modeling applications.* Environ Sci Pollut Res Int, 2020. **27**(29): p. 35873-35874.
236. Guo, D., A. Wang, and A.T. Zhang, *Pollution exposure and willingness to pay for clean air in urban China.* J Environ Manage, 2020. **261**: p. 110174.
237. Deshmukh, P., et al., *Identifying air pollution source impacts in urban communities using mobile monitoring.* Sci Total Environ, 2020. **715**: p. 136979.

238. Hien, P.D., et al., *Impact of urban expansion on the air pollution landscape: A case study of Hanoi, Vietnam.* Sci Total Environ, 2020. **702**: p. 134635.
239. Power, A.L., et al., *Monitoring Impacts of Urbanisation and Industrialisation on Air Quality in the Anthropocene Using Urban Pond Sediments.* Frontiers in Earth Science, 2018. **6**.
240. van den Brandeler, F., J. Gupta, and M. Hordijk, *Megacities and rivers: Scalar mismatches between urban water management and river basin management.* Journal of hydrology (Amsterdam), 2019. **573**: p. 1067-1074.
241. Sagripanti, J.L. and C.D. Lytle, *Estimated Inactivation of Coronaviruses by Solar Radiation With Special Reference to COVID-19.* Photochem Photobiol, 2020. **96**(4): p. 731-737.
242. Kroumpouzos, G., et al., *COVID-19: A relationship to climate and environmental conditions?* Dermatol Ther, 2020: p. e13399.
243. Gunthe, S.S., et al., *On the global trends and spread of the COVID-19 outbreak: preliminary assessment of the potential relation between location-specific temperature and UV index.* Z Gesundh Wiss, 2020: p. 1-10.
244. Yao, Y., et al., *No association of COVID-19 transmission with temperature or UV radiation in Chinese cities.* Eur Respir J, 2020. **55**(5).
245. Mobarra, N., et al., *A Review on Iron Chelators in Treatment of Iron Overload Syndromes.* Int J Hematol Oncol Stem Cell Res, 2016. **10**(4): p. 239-247.
246. Oreshkova, N., et al., *SARS-CoV-2 infection in farmed minks, the Netherlands, April and May 2020.* Euro Surveill, 2020. **25**(23).
247. Miransky, V.A., *Catalysis of dynamical symmetry breaking by a magnetic field.* Progress of Theoretical Physics Supplement, 1996(123): p. 49-59.
248. Horsten, L., *Theory and reality. An introduction to the philosophy of science.* Tijdschrift Voor Filosofie, 2005. **67**(2): p. 393-394.
249. Lehoux, D. and J. Foster, *The Structure of Scientific Revolutions, 4th edition.* Science, 2012. **338**(6109): p. 885-886.
250. Dupuis-McDonald, G., *The possibility of a logic of discovery: abduction as a philosophical model for scientific discovery.* Phares-Revue Philosophique Etudiante De L Universite Laval, 2019. **19**(1): p. 105-125.
251. Mott, N., *Postscript to the Logic of Scientific Discovery, Vol 1, Realism and the Aim of Science - Popper,K.* Contemporary Physics, 1983. **24**(5): p. 509-510.
252. van der Gucht, J., *Grand Challenges in Soft Matter Physics.* Frontiers in Physics, 2018. **6**.
253. Marx, V., *Cell biology befriends soft matter physics.* Nature Methods, 2020. **17**(6): p. 567-570.
254. Marx, V., *Cell biology befriends soft matter physics.* Nat Methods, 2020. **17**(6): p. 567-570.